DNS OF TURBULENT CHANNEL FLOW WITH INCLINED, CONTINUOUS AND SEGMENTED V-SHAPED TURBULATORS

By

John A Lucena Jimenez

A thesis submitted in partial fulfillment of the requirements for the degree of

MASTER OF SCIENCE

in

MECHANICAL ENGINEERING

UNIVERSITY OF PUERTO RICO
MAYAGÜEZ CAMPUS

May, 2011

Approved by:

R. Vikram Pandya, Ph.D Member, Graduate Committee	Date
Silvina Cancelos, Ph.D Member, Graduate Committee	Date
Stefano Leonardi, Ph.D President, Graduate Committee	Date
Paul Castillo, Ph.D Representative of Graduate Studies	Date
Gustavo Gutierrez, Ph.D Chairperson of the Department	Date

Abstract

The cooling system of the gas turbine blades plays a critical role in increasing the thermal efficiency and power output of advanced gas turbine engines. In fact, by increasing the heat transfer, the turbine blade can resist to an impinging fluid with higher temperature. Roughness elements (turbulators) are usually placed on the walls of the internal channels of a turbine blade to enhance the heat transfer.

Direct numerical simulations are carried out to study the turbulent flow in a square channel with continuous V- shaped turbulators on one wall and segmented V-shaped square ribs on two walls. The geometrical parameters are $k/h = 0.25$, $w/k = 3, 5$,$\alpha = 45, 60, 75$ and $G/H = 0.2$, where k is the rib height, w the pitch, h the channel half height, α the angle in degrees with respect to the flow direction and G the gap size (segmented V-shape only). Numerical results show that the heat transfer is 9% higher while the drag is 10% lower for the segmented V-shaped configuration ($w/k = 3$,$\alpha = 45$), when compared with that for continuous V-shaped turbulators. The drag reduction is due to the fact that turbulators have less surface perpendicular to the flow direction, and as a consequence, the form drag decreases. The heat transfer enhancement is caused by a change in the flow structure inside the cavity due to the stream through the gap.

When the turbulators are placed on one wall only, the drag and heat transfer are, respectively, 3.00 and 3.04 less than that in continuous V-shaped turbulators. By varying the angle of the turbulators with respect to the flow direction, higher heat transfer and drag is found for $\alpha = 60$ ($w/k = 5$).

Resumen

El sistema de enfriamiento de las aspas de una turbina de gas tiene un rol crítico en la eficiencia termal de la misma. Si se incrementa la transferencia de calor en una turbina de gas, esta puede resistir flujo mas caliente. Para incrementar la trasferencia de calor en estas aspas, se colocan rugosidades en las paredes de los canales de enfriamiento internos. Simulaciones numéricas directas fueron realizadas para estudiar el flujo turbulento en un canal con rugosidad en forma de V continua en una pared y rugosidad de forma segmentada en las dos paredes. Los parámetros del estudio son $k/h = 0.25$, $w/k = 3, 5$, $\alpha = 45, 60, 75$ y $G/H = 0.2$, donde k es la altura del elemento, w la distancia entre los elementos, h la altura del canal y G el tamaño del hueco (solo para el elemento segmentado). Se encontró que la rugosidad segmentada en forma de V promueve un aumento de 9% en la transferencia de calor y una reducción de 10% del arrastre total cuando se compara con los valores de la rugosidad continua en forma de V. El arrastre reduce debido a la reducción de área normal al flujo y la transferencia de calor aumenta debido a cambios en la estructura de flujo dentro de la cavidad (espacio entre los elementos rugosos). Por otra parte la transferencia de calor y el arrastre es 3 veces menos cuando se colocan los elementos rugosos en una sola pared. Cuando se varía el àngulo, la mayor cantidad de transferencia y arrastre de calor ocurre para $\alpha = 45$ ($w/k = 5$).

Copyright © 2011

by

John A Lucena Jimenez

To my family, specially my wife Grace Berrios, who gave me support and sat by my side when I was working late in the night.

ACKNOWLEDGMENTS

I would like to thank my advisor, Dr. Stefano Leonardi for giving me the opportunity of working with him since 2008. With him I learned how to fulfill my research goals and how to conduct graduate level scientific research. Also, I would like to thank all my lab partners specially Benjamin Cruz and Jaime Toro, who gave me much help in my Master's first year and their advice was important in the development of this work. Also, I would like to thank Amabel Reyes for giving me tips in how to organize my seminar presentation.

In addition, I would like to thank Pratt & Whitney for the funding of this research. Finally, I'm grateful of everyone that, in any way, gave me academic and personal support.

TABLE OF CONTENTS

LIST OF FIGURES

LIST OF ABBREVIATIONS

MPI	Message Passing Interphase
DNS	Direct Numerical Simulation
CFD	Computational Fluid Dynamics
CFL	Courant, Frederich and Levy
LES	Large Eddie Simulations
RMS	Root Mean Square

LIST OF SYMBOLS

α	Angle of incidence to the flow
C_D	Drag Coefficient
P_d	Form Drag
C_f	Skin Frictional Drag
C_{fo}	Flat Channel Skin Frictional Drag
ΔP	Pressure difference
Δt	Time step
Δx_i	Mesh width in the i^{th} direction
h	Mid-channel Height
k	Turbulators Height
w	width
G	Gap size
μ	Dynamic viscosity
Nu	Nusselt number
∇	Gradient operator
ν	Kinematic viscosity
P	Pressure
Pr	Prandlt number
Π	Body force
q	Heat flux
q_o	Flat Channel Heat flux
Re	Reynolds number
ρ	Density
T	Temperature
τ	Time constant
τ_w	Shear stress
u_i	Instantaneous velocity component in the i^{th} direction
$\bar{U}_i$	Average velocity component in the i^{th} direction
x_i	Component of coordinate in the i^{th} direction
V	Velocity
S	Symmetric tensor of velocity gradient
Ω	Antisymmetric tensor of the velocity gradient
λ_2	Second Eigenvalue
u	Streamwise velocity
w	Spanwise velocity
v	Wall normal velocity
U_b	Bulk velocity
U_c	Centerline Velocity

CHAPTER 1
INTRODUCTION

1.1 JUSTIFICATION

The study of the heat transfer in turbulent channels is of special interest in engineering applications such as in the design and development of gas turbines. Gas turbines are commonly used for power generation, aircraft propulsion and many industrial applications. Due to the current cost of fuels and to produce more environmental friendly engines, efforts are made in how to rise the efficiency of such systems. A gas turbine engine follows in good approximation the Brayton cycle. The gas turbine efficiency is directly proportional to the temperature of the working fluid impinging the turbine. Therefore, an increase of temperature would lead to a higher efficiency and lower fuel consumption. However the main problem of increasing such temperature is that turbine blades have temperature limits. To control the high operating temperatures in the blades, two cooling mechanisms are commonly used: film and channel cooling. The present research is focused on ribbed channel cooling. A sketch of a modern gas turbine blade with the position of ribbed channel is shown in fig. 1–1.

Previous studies have demonstrated that artificially roughened channels increase the overall channel heat transfer and fluid flow resistance with respect to a smooth wall channel (Leonardi et al [25]). In literature such artificial roughness geometries are commonly called rib turbulators. First studies of heat transfer enhancement using turbulators (Han [1],[2]) dealt with square or rectangular channels using square bars perpendicular to the flow. This is the most common configuration

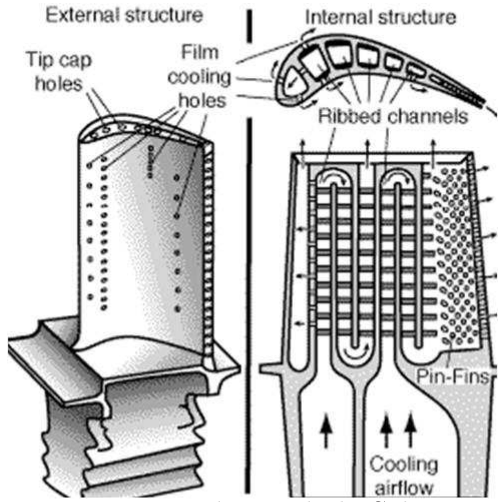

Figure 1–1: Turbine Blade Schematic

used nowadays. It was demonstrated that the heat transfer is highly dependent on the rib height k, the pitch w, the Reynolds number and the channel aspect ratio. The reason of this increase is that turbulators promote recirculation which cause more mixing of fluid particles in the channel. This motion is usually caused by vortices or vortical structures and by the bursting or ejection phenomena (Robinson [3]). The result is an increase of heat transfer transport from the walls to the fluid outer layer. Leonardi et al. [25] demonstrated in detail the relationship between the heat transfer, drag and turbulence using Direct Numerical Simulation.

Other studies demonstrated that angled rib turbulators promote more heat transfer and the ratio between heat transfer increase and the drag is larger when compared to channels with square bars ([4],[5]). This type of geometry is commonly called V-shaped (Fig 1–2) configuration. The problem with this configuration is that it cannot be manufactured in aircraft gas turbine engines with current technology. On the other hand, it can be manufactured with a small gap in the center of the turbulator (Fig 1–2) which hereafter it will be referred as Segmented V-shaped. G. Tanda [6] demonstrated that discontinuities in the turbulator can enhance the local heat transfer but the effects of this gap have not been studied yet. Also detailed flow structure and heat transfer results on both: segmented V-shaped and onewall V-shaped were not found in literature.

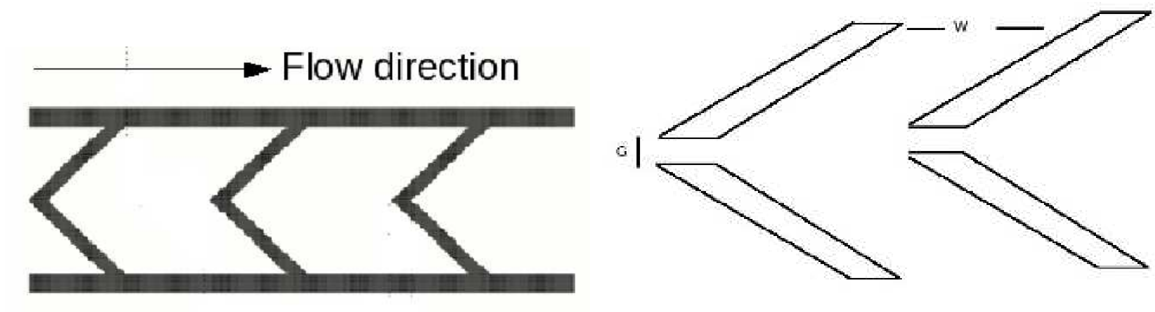

a) Non-segmented V-shaped b) Segmented V-shaped

Figure 1–2: V-shaped geometrical configurations

1.2 OBJECTIVES

The main objective of this research is to find if Segmented V-shaped turbulator are more efficient in transporting heat while requiring less pumping power when compared with continuous V-shaped turbulators. In order to complete this task the understanding of the flow structure and heat transfer was needed for the geometry in study (Fig. 1–2). The same study has to be done to compare the heat transfer and total drag between one wall and two walls V-shaped ribbed channels. In order to comply with this objective, the flow field and temperature distribution will be computed numerically and the results will be compared with the numerical database generated by Toro [33] (Continuous V-shaped). Both cases will be studied for $k/h = 0.25$, $w/k = 3.0$ and $G/h = 0.2$ for the gap size on the segmented V-shaped configuration. These parameter where chosen because previous studies of V-shaped ribs (Toro [33]) shows that the heat transfer is maximum for $k/h = 0.25$ and $w/k = 3.0$. Finally, the effects of varying the angle with respect to the flow will be studied for inclined and V-shaped turbulators with $k/h = 0.25$, $w/k = 5$ and $\alpha = 45, 60, 75$ degrees.

CHAPTER 2
LITERATURE REVIEW

2.1 WALL STRUCTURES

Turbulence has been widely studied with experiments and numerical simulations. Since the heat transfer and pressure losses are highly dependent on flow turbulence, it is important to understand what causes this phenomena. Interaction of turbulent structures inside the boundary layer promotes turbulence production. Studies of smooth wall have been done by Kim et al.[20] where they state that almost all the turbulence generation occurs during bursting in the zone $0 \leq y^+ \leq 100$ where $y^+ = v^* y/\nu$, v^* the wall-friction velocity,y the normal wall direction and ν the kinematic viscosity. The authors define the bursting process as a three-stage process of low-speed streak lift-up, oscillation and a break-up. A streak is a collection of fluid particles that pass continuously through the flow field. The streaks are observed easily in experiments by the use of dyes. It was observed that the bursting process has a 10 cycle duration. This process causes constant movement of the flow particle from the near wall to the outer layer.

There are many hypotheses about the origin of the bursting process. Most of these hypothesis state that the bursting process is associated with vortical structures oriented along the flow direction horseshoe vortices (Robinson [3]). A significant portion of studies are dedicated to detection and characterization of the vortical structures inside the boundary layer. Vortices are highly three-dimensional and they transport momentum across the mean velocity gradient (Robinson [3]).

Three-dimensional vortices are characterized more easily in numerical studies due to the fact that it is required detailed flow field data which is difficult to obtain experimentally. For example J. Jeong and F. Hussain [10] proposed a method of vortex identification based on the eigenvalues of tensor $S^2 + \Omega^2$ where S and Ω are, respectively, the symmetric and the antisymmetric parts of the velocity gradient tensor (λ_2 method). Different shapes have been proposed for the boundary layer vortices. Smith et al. [11] found steady state streamwise vortices in the near-wall end views while Clark et al. [12] observed transverse vortices in convecting and stationary side view of the outer region. Different geometries of vortical structures were referred as "arches" or "horseshoes" that appeared to be symmetrical in size and "hairpin" vortices which posses elongated trailing edges (Head et al. [13]). Moin and Kim [29] proposed that "hairpin" vortices are the dominant flow structure. They indicated that "hairpins" are formed by the deformation, stretching, and lifting of the transverse vortex. It was found that strongest vorticity vectors form at a angle of 45 degrees from the wall, similar to the angle between the hairpin vortex core and the wall.

2.2 ROUGH WALL

The present study objective is to quantify and compare the heat transfer of a roughened turbulent channel. For this reason, the wall boundary conditions becomes more complex. The flow details depends on the geometrical configuration of the roughness elements and the viscous sub-layer is different when compared to a smooth wall.

Perry et al. [30] studied the turbulent boundary layer of transverse roughened wall and proposed a roughness type division. He categorized the roughness as k-type and d-type. The letters d and k denotes the significant length scale that characterizes the velocity profile, friction factor and determines the roughness function. The k refers to the roughness height and d to the boundary layer thickness, pipe diameter or channel height.

It is well established that a source of turbulent energy is the mean shear. This means that energy supply depends on the surface nature (Djenidi et al. [14]), therefore the turbulence generation of rough surfaces will be different with respect to a smooth wall. The roughness affects the mean velocity profile causing a displacement or shift inside the logarithmic region. This shift is what defines the roughness function ΔU^+. Leonardi et al. [15] found that the difference between k-type and d-type roughness for channel flow is related to the magnitudes of frictional and pressure drag. In fact, the frictional drag dominates over the pressure drag for a d-type behavior roughness, whereas the pressure drag is dominant for k-type roughness. The d-type roughness transition was found to be for $w/k = 1$. L.Keirsbiuck et al. [16] found that the effects of d-type roughness on the Reynolds stresses are confined in the near wall region and k-type roughness promotes more violent ejections.

The present works deals with the study of V-shaped square ribs turbulators. A more simple approach to this problem, is to study the effect in the flow structure and velocity profiles for transverse square ribs roughness. Cui et. al [34] studied this type of roughness geometry by the use of Large Eddy simulation (LES). In this paper, the Navier Stokes equations were solved using a Cartesian coordinates, and the sub-grid scales were modeled with a dynamic-sub-grid-scale model. They found that, for d-type roughness, the interaction between the outer flow and the roughness layer is minimal. For intermediate roughness, the outer flow is affected by the large turbulent eddies ejecting form the cavity, but there is no flow reattachment. For k-type roughness, there is more interaction between the eddies in the cavity and the outer flow, and there is flow separation and reattachment inside the cavity. This reattachment is what promotes more interaction between the flow in the cavity and the outer layer. Leonardi et. al. [24] demonstrated the advantage of using direct numerical simulation to study square rib roughness. With direct numerical simulations, the variables such as pressure and velocities are known in all the grid points. With this information, the pressure distribution is known around the roughness and the form drag is easily calculable. This is very difficult to obtain experimentally. They also found that there is a direct relationship between the total drag and the roughness configuration (w/k). In fact, the minimum friction and maximum pressure drag occurs when the flow reattachment occurs just before the roughness element ($w/k > 7$). For the case of one wall ribbed channels, Leonardi et al [7] demonstrated that the roughness function is independent of the upper wall boundary conditions but there is a shift upward of the velocity maximum if scaled in normal units.

A roughness configuration that resembles more closely to this thesis work, is that of 45 degrees transverse ribs. S.Y. Won & P. M. Ligrani [8] performed experiments in a channel with angled crossed-rib turbulators. They found evidence of strong secondary flow and large spanwise velocity gradients near the wall. The strong secondary motion in the spanwise direction followed the direction of the rib and increases with the Reynolds number. Also, major losses of total pressure and deficits of streamwise velocities are larger in the channel center [8]. Tachie et. al. [9] conducted experiments on a turbulent channel with periodic 90 and 45 degrees transverse and inclined ribs. They were able to measure turbulence statistics and plot profiles and contours of the mean velocity. They found that secondary motions promoted inside the cavity of the 45 inclined ribs caused changes in the mean velocity profile by flattening the streamwise velocity in the outer layers. For this reason, there is a reduction in the turbulence and drag over the 45 inclined ribs when compared with the transverse ribs. It was also shown that this secondary motion caused a change in the flow structure throughout the channel.

2.3 RIB-ROUGHENED CHANNEL HEAT TRANSFER AUGMENTATION

First studies heat transfer augmentation in channel flows date back to mid 1960's [17]. Most of these studies dealt with uniformly heated square or rectangular channels with walls roughened by ribs. The most common geometry studied were the continuous regularly spaced, transverse square bars ([1],[2]).On such studies, different researchers found that the most important parameters that affect the heat transfer and pressure drop were the rib pitch p to height e ratio, channel aspect ratio,the flow Reynolds number and hydraulic diameter D. The parameters relationship that most affects the heat transfer and pressure drop are the pitch over the rib height and the rib height over the hydraulic diameter. Researchers found that heat transfer and pressure drop were maximum for $p/e = 6 - 15$ for $e/D = 0.004 - 0.063$. The maximum heat transfer occurs for those p/e because of the flow structure between the roughness elements. At lower p/e the flow separates after the ribs but it does not reattach in the cavity, contrary to large p/e where flow reattaches and there is boundary layer formation. In others studies it was demonstrated that parallel angled ribs provided better heat transfer performance when compared with transverse ribs. The rib angle induces a secondary flow, which follows the rib direction resulting in an increase of heat transfer performance per unit friction. Han et al. [18] discovered that 45 degrees angled rib produced an optimum thermal-hydraulic performance; much better than the transverse ribs. Since placing the ribs with an angle with respect to the flow induces flow turbulence and enhances the thermal-hydraulic performance, further experiments were performed with the V-shaped arrangement. There are two types of V-shaped configurations encountered in literature: with the V pointing downstream and the V pointing upstream. The V pointing downstream configuration is often call lambda configuration while the upstream pointing is called V-shaped configuration. Han et al. [4] found that 45-60 degrees V-shaped ribs performed better than angled or transverse ribs. The V-shaped ribs performed better when pointing upstream rather than downstream. Han et al. [19] also found that broken V-shaped ribs offered higher heat transfer, compared to continuous V-shaped ribs. It is important to clarify that the author refers to broken as complete V-shaped ribs separated in the spanwise direction. The study proposed on this thesis refers to a single V-shaped rib configuration with a small gap or discontinuity (See fig. 1–2).

Tanda [32] performed experiments to compare the performance between 45 degrees inclined ribs placed on one wall and both walls. He found that the ratio of the friction factors (f/f_o) is about three times higher when both walls are roughened. f and f_o are, respectively, the roughened and flat wall channel friction factor. He also observed that the heat transfer augmentation ranged from 1.6 to 2.25 for the one wall ribbed channel case and ranged from 1.85 to 2.55 for the both walls ribbed channel case.

Toro [33] performed Direct Numerical Simulations on continuous V-shaped ribbed channels in order to find an optimum configuration for heat transport and determine the total drag. He found that the configuration that promotes the most heat transfer is $w/k = 3$ and $k/h = 0.25$. He observed that, for V-shaped turbulators, a secondary motion is produced by the roughness which leads to large ejections on the side walls. This ejections will interact and generate a streamwise large scale vortex. This large ejections are the key of the heat transfer augmentation produced by this roughness configuration. The database that he generated has been used in this work in order to compare the thermal performance of each configuration.

The change of the roughness angle with respect to the flow influence the channel drag and heat transfer. For narrow aspect ratios channels, the pressure drop penalties are 2 o 4 times for the 45 and 60 degrees angeled ribs and can be as high as 8 to 16 times for broad-aspect ratio channels, all with respect to smooth channel [22]. Results also shows that 60 degrees angeled ribs provide the best heat transfer augmentation for narrow and broad aspect ratio channels [22].

CHAPTER 3
NUMERICAL METHOD

Direct Numerical Simulation of the turbulent channel flow with V-shaped turbulators has been performed.

The incompressible Navier-Stokes equations are solved to obtain the pressure and velocity at each grid point. The non-dimensional Navier-Stokes and continuity equations for incompressible flows are:

$$\frac{\partial U_i}{\partial t} + \frac{\partial U_i U_j}{\partial x_j} = -\frac{\partial P}{\partial x_i} + \frac{1}{Re}\frac{\partial^2 U_i}{\partial x_j^2} + \Pi\delta_{i1} \ , \qquad \frac{\partial U_i}{\partial x_i} = 0 \tag{3.1}$$

where Π is the pressure gradient required to maintain a constant flow rate, δ_{ij} is the Kronecker delta, U_i is the i^{th} component of the velocity vector direction, x_i is the dimension vector in the i^{th} direction, P is the dimensionless pressure given by $P_*/(\rho U_c^2)$, Re is the Reynolds number obtained from $U_c h/\nu$ and t is the dimensionless time given by $t_* U_c/h$. The variables with * represent a dimensional unit, ν is the kinematic viscosity, U_c is the centerline velocity and h is the channel half height.

To find the temperature distribution and heat flux the non-dimensional energy equation was solved across the domain:

$$\frac{\partial T}{\partial t} + \frac{\partial T U_j}{\partial x_j} = \frac{1}{Re\ Pr}\frac{\partial^2 T}{\partial x_j^2} \ , \tag{3.2}$$

where T is the temperature and $Pr = \nu/\alpha$ is the Prandtl number.

To solve numerically the Navier-Stokes (Equation 3.1) and Energy Equation (Equation 3.2) the domain has been discretized in an orthogonal coordinate system using the staggered central second-order finite-difference approximation. Here, only the main features are recalled since details of the numerical method can be found in Orlandi [26] and Leonardi & Orlandi [27]. The discretized system is advanced in time using a fractional-step method with viscous terms treated implicitly and convective terms explicitly. The large sparse matrix resulting form the implicit terms is inverted by an approximated factorization technique. At each time step, the momentum equations are advance with the pressure at the previous step, yielding an intermediate non-solenoidal velocity field. A scalar quantity Φ projects the non-solenoidal field onto a solenoidal one. A hybrid low-storage third-order Runge-Kutta scheme is used to advance the equations in time (Wray [21]).

Stability of the numerical scheme is achieved by imposing the Courant, Friedrich and Levy (CFL) condition given by:

$$\frac{u_i \Delta t}{\Delta x_i}|_{max} < 1, \tag{3.3}$$

where Δt is the time step and Δx_i is the mesh width in the ith direction. The physical meaning of this condition is that a fluid particle should not cross the grid space in one time step.

Another stability condition must be satisfied when the linear terms are treated explicitly:

$$\frac{\Delta t}{\Delta x^2 Re} < \frac{1}{2n}, \tag{3.4}$$

where n is the number of dimensions (2 for 2D and 3 for 3D). This condition is analogous to the Fourier number, which is the stability condition when solving the heat equation explicitly. Since in our numerical method linear terms are discretized implicitly condition 3.4 is automatically receded.

The roughness is treated by the efficient immersed boundary technique introduced by Fadlum et. al. [31] and modified later by Orlandi & Leonardi [27]. This

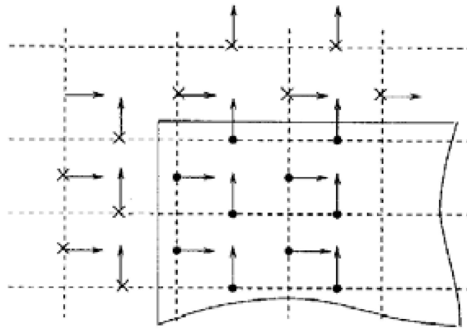

Figure 3–1: Geometrical sketch of immersed boundary method. Arrows, velocity vectors as defined in a staggered grid. Solid line delineates a roughness element and the dashed lines defines the grid

approach allows the solution of flows over complex geometries without the need of computational intensive body-fitted grids. This method is ideal to solve the flow field around complex roughness elements. It consists of imposing $U_i = 0$ on the body surface, which does not necessarily coincide with the grid (See fig 3–1). To avoid that, the geometry is described in a stepwise way, at the first grid point outside the body, the second derivatives in the Navier-Stokes equations are discretized using the distance between the velocity and the boundary of the body rather than using the mesh size (See arrows of Fig. 3–1).

Periodicity is applied in the spanwise and streamwise directions of the computational box. To set this condition, the values u_i and T must be equal at the grid points $x = 0, z = 0$ and $x = max, z = max$. No-slip conditions is set at the top and bottom wall and on the rough surfaces.

The Reynolds number $Re = U_c h/\nu$ is 10400, while the Prandtl number Pr is set equal to 1; where, U_c is the centerline velocity, ν the kinematic viscosity and h the channel half height. The computational box is $6h \times 2h \times 2h$ in the streamwise, normal and spanwise direction respectively. A non-uniform grid is used in the y direction to capture the flow structure inside the cavity and the steep gradients at the wall. Fig 3–2 shows the distribution of the grid in the y direction. The total number of nodes in the y direction is 192, where 50 nodes are clustered inside each cavity. The number of nodes in the spanwise and streamwise direction is 192

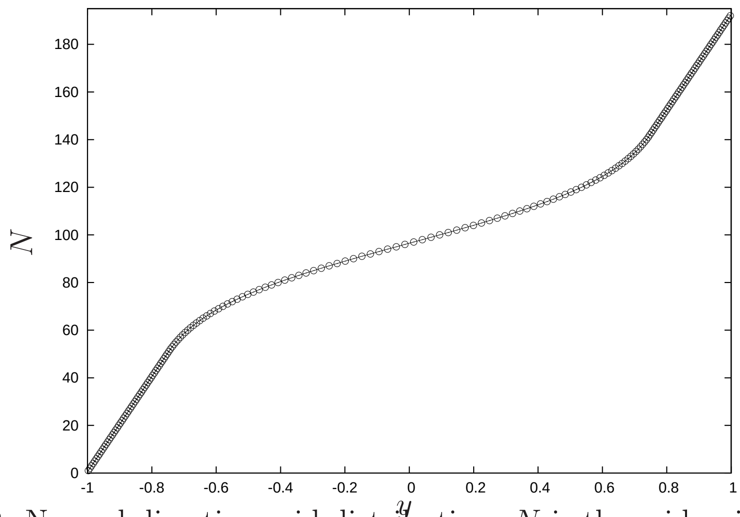

Figure 3–2: Normal direction grid distribution. N is the grid point number.

and 640 respectively. This yields a grid 640 (482 for inclined turbulators) x 192 x 192 with about 24 million points. The solution in time is very expensive in terms of computational resources. To resolve the discretized equations on such a grid is necessary to use parallel computing.

When a code is run on a parallel computing cluster using n nodes the computational domain is divided into n sub-domains and each node solves only one sub-domain (See Figure 3–3). Since our method is implicit and the set of equations is elliptic in space, the nodes have to communicate and transfer velocity and pressure at the border of each sub-domain.

The simulations have been performed on "Ranger", a cluster of the Texas Advanced Computing Center (TACC) and on our in-house cluster.

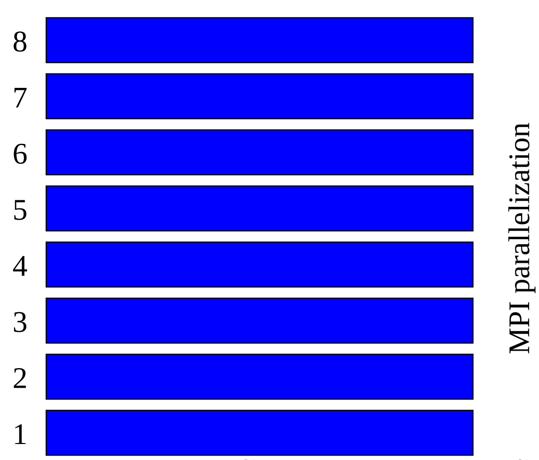

Figure 3–3: Layered Computational Box Sketch

3.1 CODE PERFORMANCE

The code has been tested on ”ranger” (of Texas Advanced Computing Center) for different grids and number of processors. The code was compiled using ”mpif90” with the option ”-r8 -O3”. The timing was obtained with the MPI function ”start-time = PMPI_Wtime()”.

```
      starttime = PMPI_Wtime()
c solution of Navier Stokes equation with a 3 step Runge Kutta
...............
...............
      endtime   = PMPI_Wtime()
      write(8,100) n,endtime-startime
```

The grids used to test the scalability of the code were:

- $128 \times 128 \times 128$
- $256 \times 256 \times 256$
- $512 \times 512 \times 512$

For each grid, a short simulation was performed using 16,32 and 64 processors. The averaged time necessary to complete one time step is shown in figure 3–4 for the different grids used. We define efficiency the ratio

$$\eta = \frac{16 t_{16}}{n_{procs} t_{procs}};, \tag{3.5}$$

where t_{16} is the time relative to 16 processors, n_{procs} is the generic number of processors for which we compute the efficiency t_{procs} is the time needed to complete an iteration using n_{procs} processors. Using 32 cores, the efficiency is about $0.64, 0.69, 0.9$ for the grids 128^3, 256^3, 512^3 respectively. Using 64 cores, the efficiency is about $0.25, 0.56, 0.85$ for the grids 128^3, 256^3, 512^3 respectively. The larger the computational box, the higher is the efficiency of the parallelization. When the computational grid is 128^3, the clock time (time you actually wait to perform the simulation) is

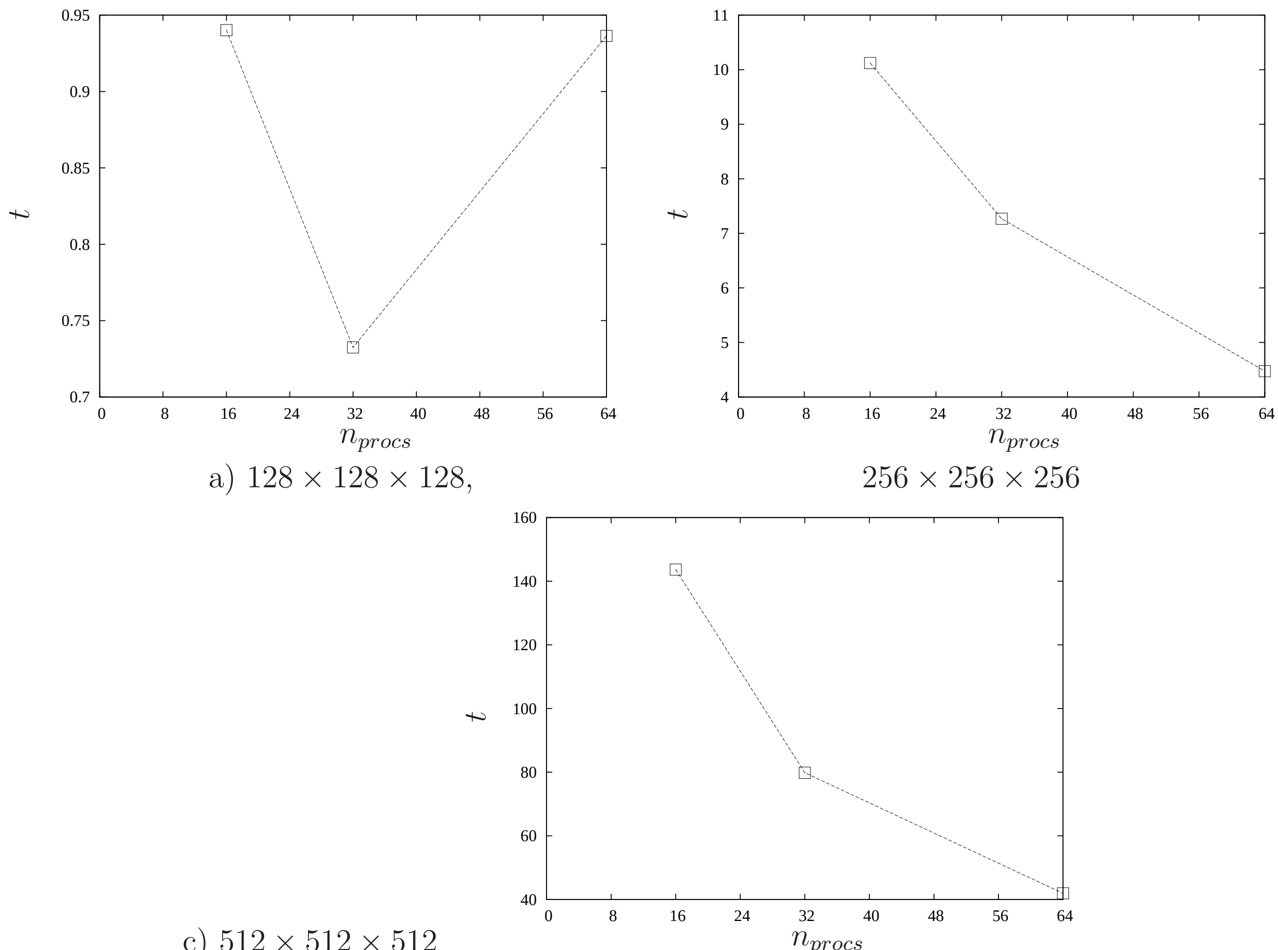

a) $128 \times 128 \times 128$, $256 \times 256 \times 256$

c) $512 \times 512 \times 512$

Figure 3–4: Computational time (t) to solve 1 step of the Navier Stokes equations as a function of the number of processors used (n_{procs}) for the computational box: a) 128^3, b) 256^3, c) 512^3.

almost the same using 16 or 64 cores. Using 64 cores the clock time is even larger than that using 32 cores. In fact, when the grid has 128^3 points, the layers in which the computational domain is divided are $128 \times 2 \times 128$. Therefore the communication between the nodes is large being both grid points in the node boundary points. For each grid point, a send-receive is necessary to compute the derivatives.

CHAPTER 4
SEGMENTED V-SHAPE

4.1 FLOW CONFIGURATION

Turbulators on the walls are made of two separate straight ribs inclined with respect to the flow direction of an angle $\alpha = 45$. Instead of having a continuous V-shaped turbulator, a gap (G) is left in the middle (see Fig 4–1). The flow configuration is $k/h = 0.25$, $w/k = 3$ and $G/h = 0.2$, where k, h, w and G stands for rib height, channel half height, pitch and gap size respectively. The temperature on the lower walls is $T = 1$ while on the upper wall is $T = -1$. Therefore heat is transported away from the lower wall and dissipated on the upper wall. The Reynolds number $Re = \frac{U_c h}{\nu}$ is 10400, while the Prandtl number Pr is equal to 1; here, U_c is the centerline velocity and ν is the kinematic viscosity, h the channel half height. The computational box is $6h$ x $2h$ x $2h$ in z (streamwise), y (wall-normal) and x (spanwise direction) respectively. Periodic boundary conditions apply in the streamwise and spanwise direction. In the vertical direction a non uniform grid was used with 192 grid nodes. Mesh sizes in the other two directions are uniform with 192 points in spanwise direction and 640 in streamwise direction, yielding typically about 24 million nodes within the domain. The database done by Toro [33] for continuous V-shaped ribs is used as a comparison.

4.2 FLOW STRUCTURE

Velocity vectors superimposed to wall normal velocity in a horizontal plane at the crest section are shown in Figure 4–2. continuous V-shaped turbulators from Toro [33] are shown as reference. In a segmented V-shaped configuration, on the

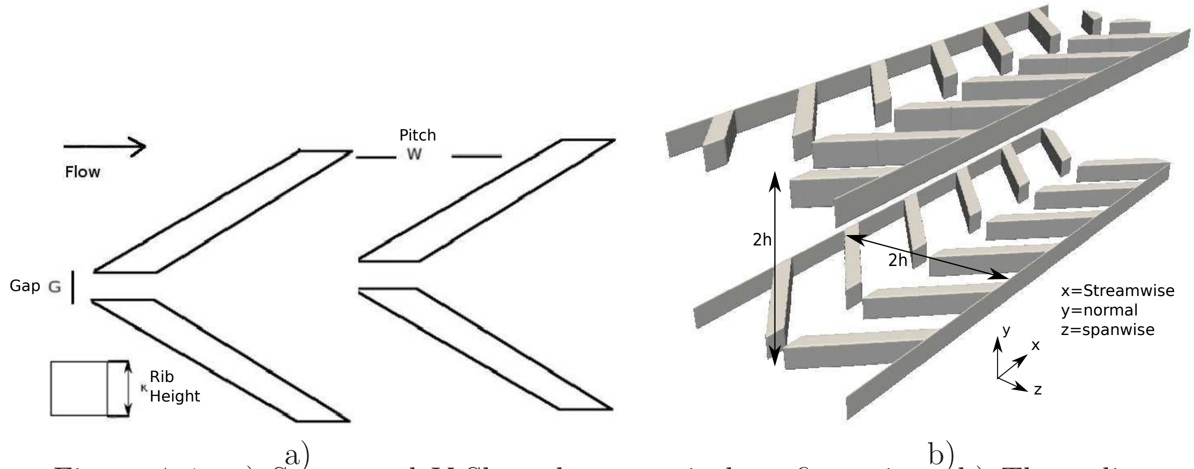

Figure 4–1: a) Segmented V-Shaped geometrical configuration. b) Three dimensional view of the flow configuration

wall there is a streak aligned with the flow direction with no obstacles. When the flow enters into the cavity formed by the turbulators one stream follows this streak, and two other streams go towards the sidewalls following the inclination of the turbulators (45 degrees). When these two streams reach the sidewalls, two ejections occur due to conservation of mass similarly to continuous V-shaped channels. The stream within the gap of the segmented V-shaped reduces the flow entering into the cavities and the ejection of the flow at the sidewall is weaker compared to that for continuous V-shaped.

The mean (average in time and streamwise direction) flow structure for segmented and continuous V-shaped turbulators is very similar. Near the sidewalls, ejections occur at the corners of the channel (see Fig 4–3). The ejections for the continuous V-shape are more intense than for the segmented V-shaped turbulators. In the center of the channel, an increase in downward velocity is observed which means that the flow is entering into the cavities of the turbulators. Similar effect is observed on the opposite walls due to the symmetry of the turbulators.

An increase of the spanwise velocity is observed near the upper and lower walls (Figure 4–4). Due to the inclination of the turbulators, the streams are tilted towards the side walls. At the side walls, after ejections occur, the flow is pushed towards the

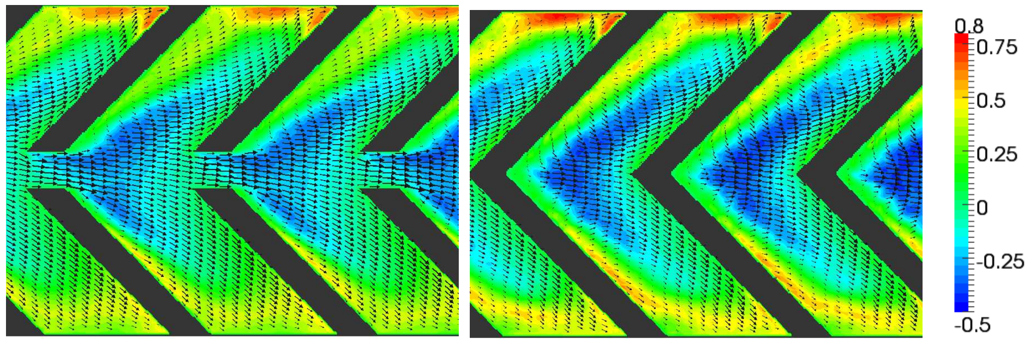

a) b)

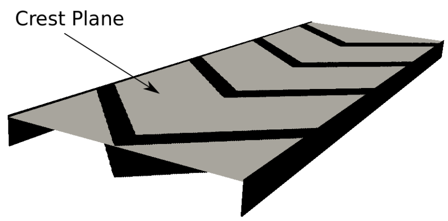

c)

Figure 4–2: Velocity vectors superimposed to time averaged wall normal velocity at the crest plane for a)Segmented V-shaped and b) Continuous V-shaped from Toro [33]. c) Crest plane

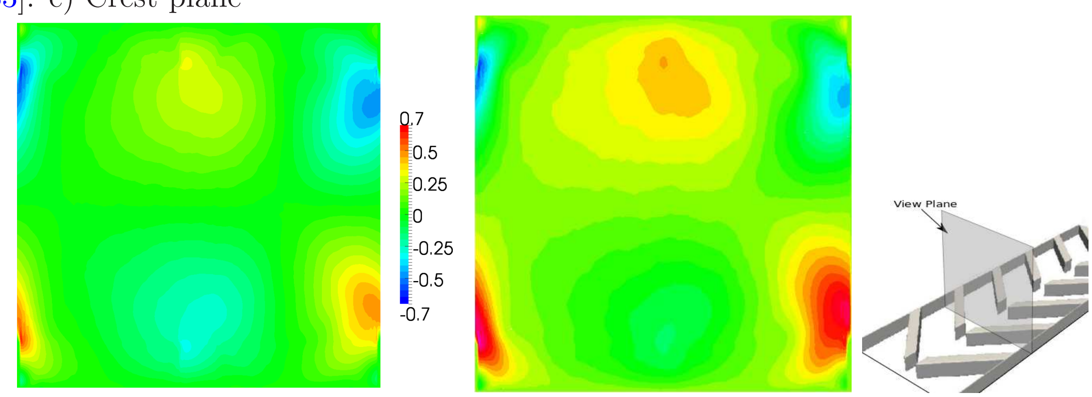

a) b) c)

Figure 4–3: Color contours of normal wall velocity averaged in time and streamwise direction for a) Segmented V-shaped and b) Continuous V-shaped (Data from Toro [33]), c) Plane normal to the streamwise direction.

center to replace the fluid entered into the cavities. The difference between broken and continuous turbulators lies in the intensity of the spanwise motion. Inside the cavity, the continuous V-shaped configuration spanwise velocity is higher. In fact, part of the mass entered into the cavities follows a straight path in the center of the bottom wall and does not contribute to spanwise motion and ejections.

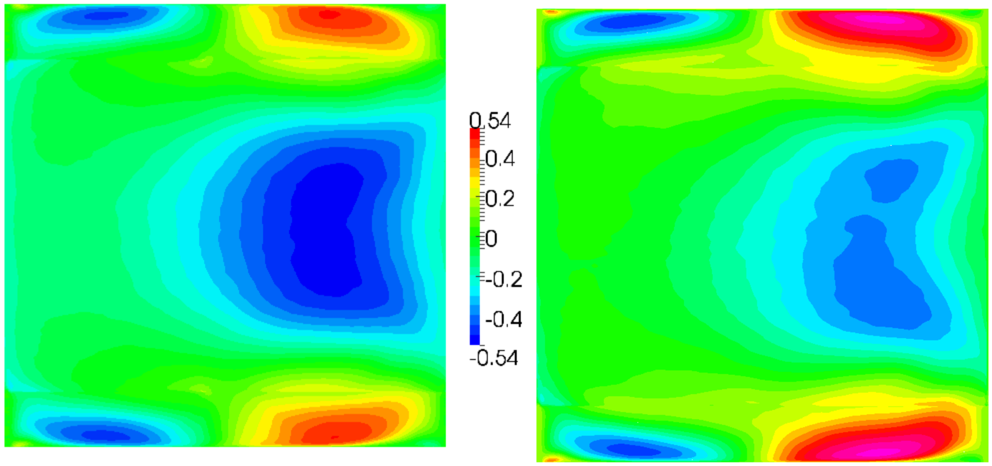

a) b)

Figure 4–4: Color contours of spanwise velocity averaged in time and streamwise direction for a) Segmented V-shaped and b) Continuous V-shaped (Data from Toro [33]).

4.2.1 Streamtraces

Since the segmented V-shaped turbulators present a gap in the center of the channel, in proximity of what would be a kink for a continuous V-shaped turbulator, particles find a street without obstacles aligned with the streamwise direction. Therefore, once the particles pass through the gap, they follow 3 different directions. One stream follows the street without obstacles at the axis of the channel. Two other streams go towards the sidewalls following the inclination of the turbulators (45 degrees) (see fig. 4–5a). When these two streams reach the sidewalls, two ejections occur due to conservation of mass similarly to what happen for continuous V-shaped. Two dimensional streamlines near the wall show that the two streams going towards the sidewall produce a separation near the gap of the turbulators (see the red arrows in fig 4–5b). These separated regions are not found in a continuous V-shaped turbulator.

4.2.2 Instantaneous streamtraces

As explained earlier, fluid particles follow three different directions when they pass trough the gap of the turbulator. On the other hand, for the continuous V-shaped turbulators, all the particles enter into the cavity from the outer layer. The

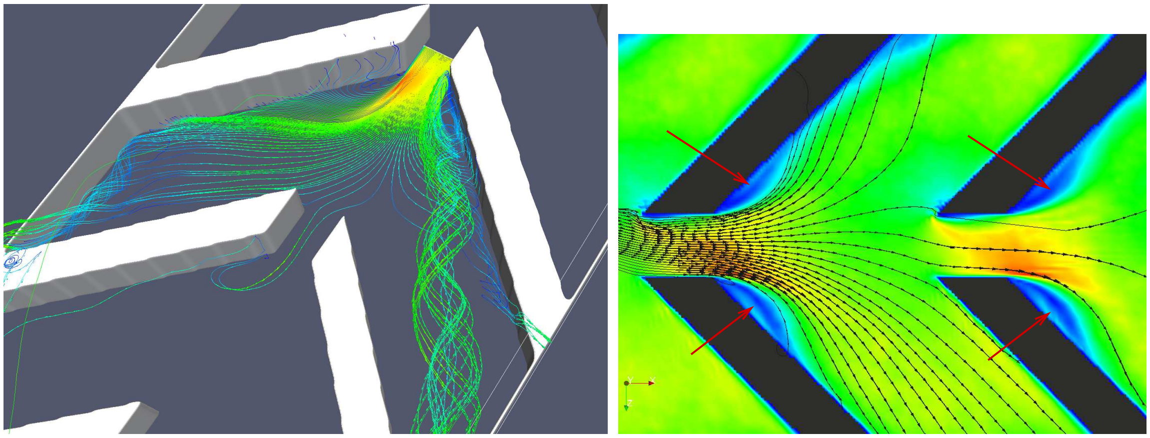

a) b)
Figure 4–5: a) Time averaged streamtraces and b) Near wall 2D streamlines; with velocity magnitude color scales.

gap affects the flow structure inside the cavity and weakens the recirculation behind each rib element. This is well appreciated in Figures 4–6 a and b. In these figures, the instantaneous streamtracers are visualized for both configurations where the color denotes the temperature at that point. In addition, the lack of strong recirculation in the segmented V-shaped turbulators, allow fluid particles to exit more quickly from the cavity and, by consequence, the flow temperature inside the cavity is lower than that in continuous V-shaped turbulators.

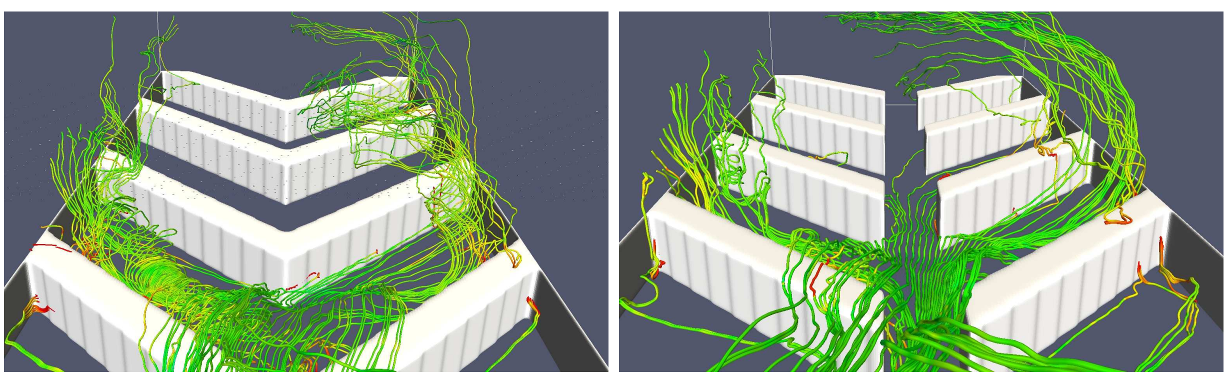

a) b)
Figure 4–6: a) Instantaneous streamtraces for continuous V-shaped configuration (Data from Toro [33]); b) Instantaneous streamtraces for segmented V-shaped configuration with temperature color scale

4.2.3 λ_2 Visualization

The second eigenvalue technique (λ_2) was used in order to properly visualize the vortical structures behind each rib element. This technique was proposed and proven by Jeong and Hussian [10]. Reffer to appendix A.1 for a detailed explanation of the calculation and implementation of the λ_2 method. The approach consist in calculating the eigenvalues of the symmetric and asymmetric velocity gradient tensor $(S^2 + \Omega^2)$. This is done in order to identify the vortex core by capturing the pressure minimum due to the vortical motion. It is considered that when the second eigenvalue (λ_2) is less than zero, a vortex core is present. When an iso-surface is drawn with a $\lambda_2 < 0$, the vortex core can be appreciated as the connected region of this certain value. The visualization of the vortex core for both geometrical configurations is shown in Figure 4–7. With this visualization method, it is confirmed that the recirculation downstream of each turbulator is weaker for segmented V-shape ribs for the reasons explained in previous sections. Also there is an elongation of this vortical structure due to the flow entering from the upstream cavity.

Figure 4–7: a) Continuous V-shaped λ_2 visualization (Data from Toro [33]); b) Segmented V-shaped λ_2 visualization;

4.3 FLOW STATISTICS

Figure 4–8 shows a plot of the time averaged streamwise velocity profiles along the normal direction for continuous ribbed V-shaped and segmented ribbed V-shaped channels. The flat channel average velocity is shown as a reference. Since the case in study is for $k/h = 0.25$, the crest plane is located at $y = \pm 0.75$. The inflection points are the same for both cases. On the other hand, there are differences on the magnitude of the streamwise component of the velocity in the near-wall region and the center of the channel. Near the wall, the velocity relative to segmented V-shaped ribbed channel is higher. This difference is expected because of higher momentum flow inside the gap of the turbulator. On the contrary, the average streamwise velocity is higher on the center of the continuous V-shaped ribbed channel. This is due to higher intensity sidewall ejections provoked by the continuous V-shape configuration. The ejections causes a spanwise motion of the flow on the center of the channel and, by continuity, the streamwise velocity has to increase.

The average streamwise velocity near the wall is similar for the flat channel and the segmented V-shaped channel. Unlike the continuous V-shaped channel, there is a streamwise flow stream inside the cavity of the segmented V-shaped turbulator allowing the formation of a boundary layer similar to that in an Flat channel. The average streamwise velocity of the Flat channel outer layer is lower than that in both V-shaped configurations. This is expected because, for a flat channel, there are not sidewalls ejections; the interaction between the flat wall and the outer layer is due only to the bursting process.

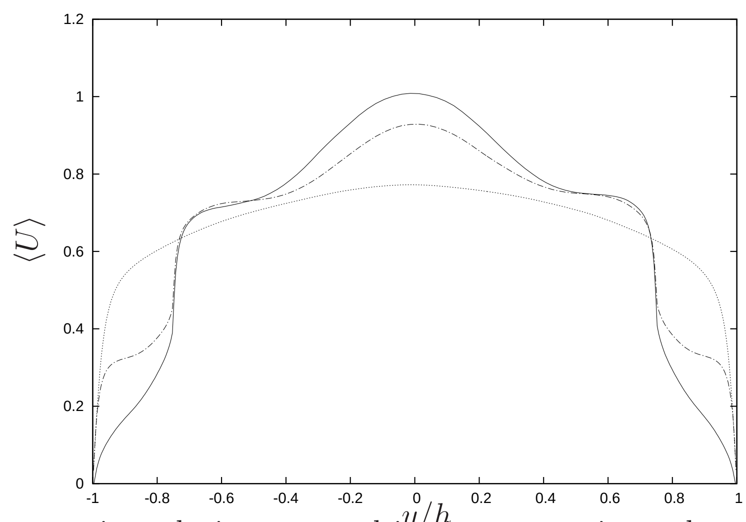

Figure 4–8: Streamwise velocity averaged in time, spanwise and streamwise direction: —·— segmented V-shape; —— , continuous V-shape (Data from Toro [33]); ········ , Flat Channel.

Figure 4–9a shows the streamwise velocity turbulent intensity profiles along the normal-wall direction for continuous ribbed V-shaped and segmented ribbed V-shaped channels. The turbulent intensity for a flat channel is shown as reference. Results show that the streamwise turbulent intensity is higher in the near wall region, inside the cavity for the segmented V-shaped rib geometry. This increase is due to the interaction of the normal wall and streamwise structures of the flow on the gap of the turbulators. In addition, the increase in streamwise turbulent intensity in the segmented V-shaped cavity is partly due to a greater mean streamwise velocity gradient near the wall caused by the presence of the turbulator gap. The magnitude is also higher on top of the crest plane. At this position there is an interaction between the streamwise large scale vortex and the high momentum flow produced by the gap in the turbulator. On the other hand, the streamwise velocity fluctuations for the continuous V-shaped turbulator geometry are higher than those recursive to the segmented V-shaped turbulator when $-0.7 <= y <= -0.3$ or $0.3 <= y <= 0.7$. In the previous mentioned region, the fluctuations are due to the unsteady streak entering the cavity from the inner channel. Since all the flow that enters the continuous V-shaped cavity comes from the inner channel, contrary to the segmented V-shaped turbulators (Fig 4–2), streamwise velocity fluctuation near the top of the crest plane has to be higher for the continuous V-shaped turbulators.

Figure 4–9b shows the normal velocity turbulent intensity profile along the normal-wall direction for both rib configurations. The normal turbulent intensity is slightly higher inside the cavity up to $y = 0.2h$ for continuous V-shaped turbulators. This difference explained by the presence of strong recirculation inside the cavity for continuous V-shape ribs. On the other hand, the normal velocity turbulent intensity is greater for the segmented V-shaped ribs from $0.2h < y < h$. Due to the large scale streamwise vortex, fluid particles move from the outer layer to the cavity. The presence of the gap in the turbulator attracts particles from the outer layer

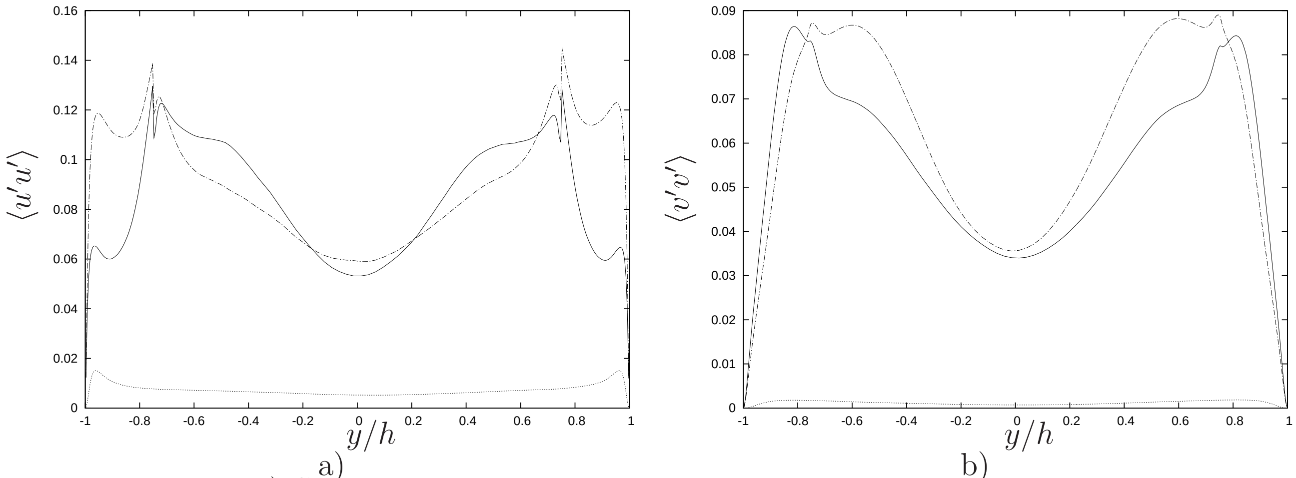

Figure 4–9: a) Streamwise velocity turbulent intensity statistics in time, spanwise and streamwise direction; b)Normal velocity turbulent intensity statistics in time, spanwise and streamwise direction : —·— segmented V-shape; —— , continuous V-shape (Data from Toro [33]); ········ , Flat Channel.

and promotes more flow interaction between the outer layer and the cavity, when compared with continuous V-shape turbulators. This interaction can be appreciated in Fig 4–6.

As expected, the streamwise and normal turbulent intensities are much lower for a flat channel. Roughness on the wall, in fact, promotes mixing (Leonardi et. al. [15]). The fluctuations on a flat wall are due to turbulent structures generated at the wall due to wall velocity gradients. On the other hand, fluctuations from V-shaped channel are due to flow separation, side wall ejections and spanwise secondary motion inside the cavity.

4.4 DRAG

4.4.1 Skin Frictional Drag

The averaged non-dimensional viscous shear stress across the streamwise direction is shown in Fig. 4–11,4–12 for the two sections (Secc CC & BB) indicated in figure 4–10. The average non-dimensional viscous shear stress $\langle C_f \rangle$ is defined as

$$\langle C_f \rangle = \frac{1}{Re} \frac{\partial \langle U \rangle}{\partial y} |_{y=0} \tag{4.1}$$

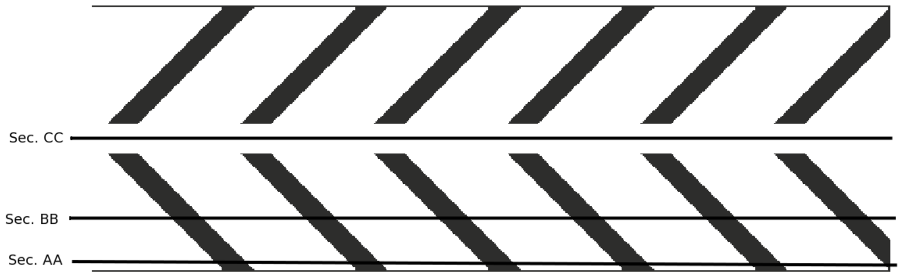

Figure 4–10: Top view geometry with labeled cross-sections

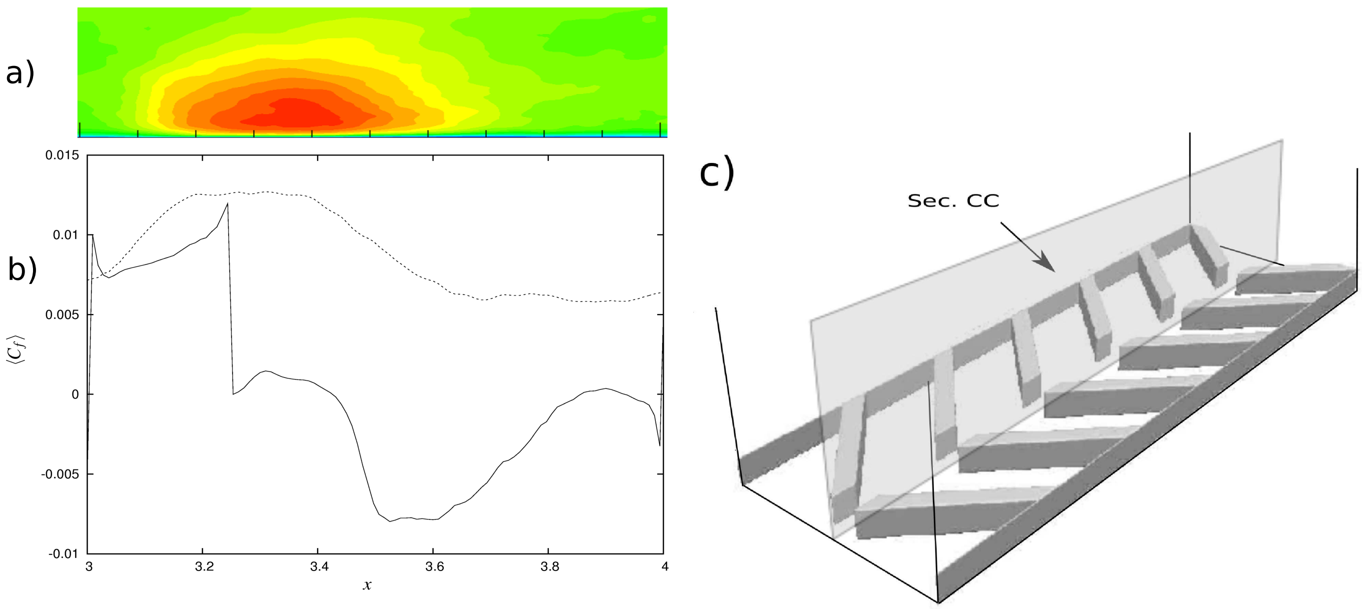

Figure 4–11: a) Time averaged streamwise velocity (shown as reference), b)Friction coefficient $\langle C_f \rangle$ averaged in time (Sec. CC): ---- , segmented V-shape; —— , continuous V-shape (Data from Toro [33]), c) Section CC view plane.

The profile presenting mayor differences between continuous and segmented V-shaped turbulators is for sec. CC. This is expected because sec. CC corresponds to the position of the gap on the segmented V-shaped turbulators configuration (fig.4–11). At the crests plane of the continuous V-shaped turbulator, the viscous shear stress is lower than that for segmented turbulators. Sec. CC for the broken turbulators represent a simple flat wall, with some flow inrush (flow towards the wall coming from the outer layer). Therefore, the friction is rather uniform which follows a parabolic trend with the peak inside the gap. On the other hand, continuous turbulators present a peak of friction at the crest and recirculation on the bottom wall within the cavity formed by two consecutive turbulators. Due to the separated regions behind the rib, a negative shear stress is observed in most of the domain and it is not present on segmented V-shape turbulators. As a consequence the frictional drag for the broken turbulators, in this particular section is higher than that for continuous turbulators.

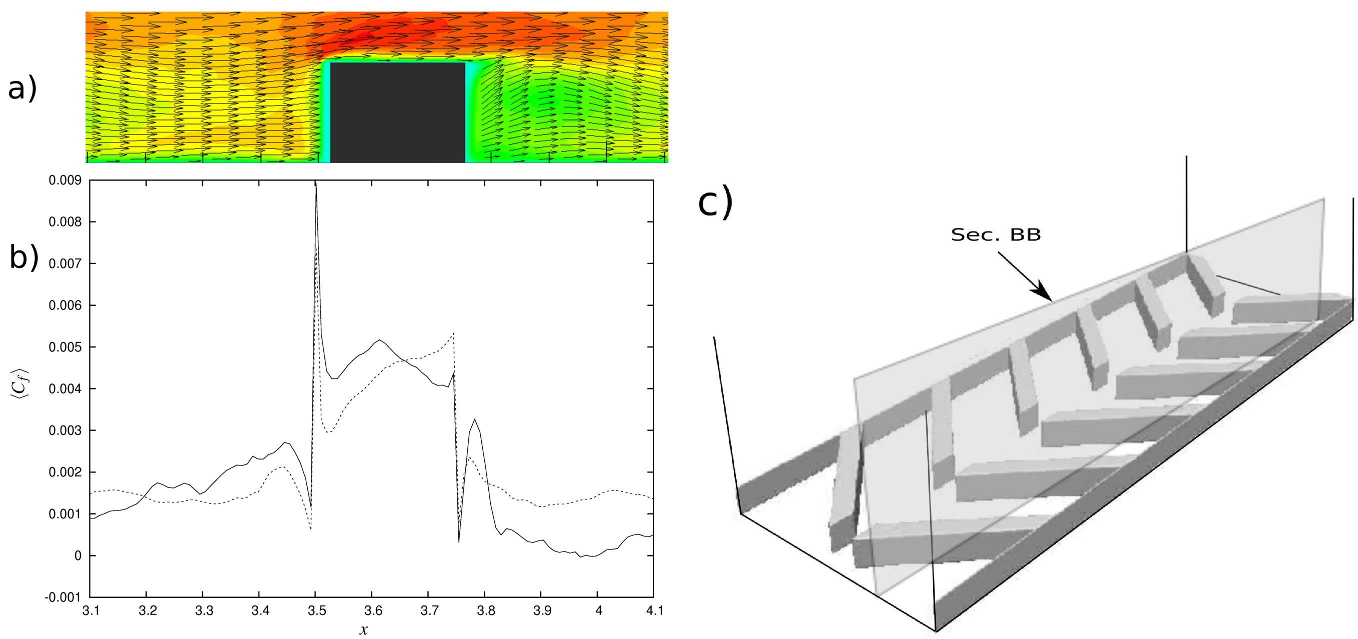

Figure 4–12: a) Time averaged streamwise velocity (shown as reference), b)Friction coefficient $\langle C_f \rangle$ averaged in time (Sec. BB): ---- , segmented V-shape; —— , continuous V-shape (Data from Toro [33]), c) Section BB view plane.

In sec. BB (fig. 4–12) the average shear stress profile is similar for both configurations. The noticeable difference lies on the cavity. The shear stresses behind the continuous V-shaped turbulators drops almost to zero and remains positive for the segmented turbulator counterpart. In fact, there is no presence of spanwise circulation behind the rib of the segmented geometry.

4.4.2 Form Drag

The form drag is directly related to the pressure exerted on the roughness surfaces. Since the roughness elements are obstructing the flow, the pressure of the surfaces where the flow impinges and the surfaces in the back of the rib is unequal; the pressure of the frontal surface has to be higher. This is similar to what is observed in studies of flow over bluff bodies. By consequence, the force exerted in

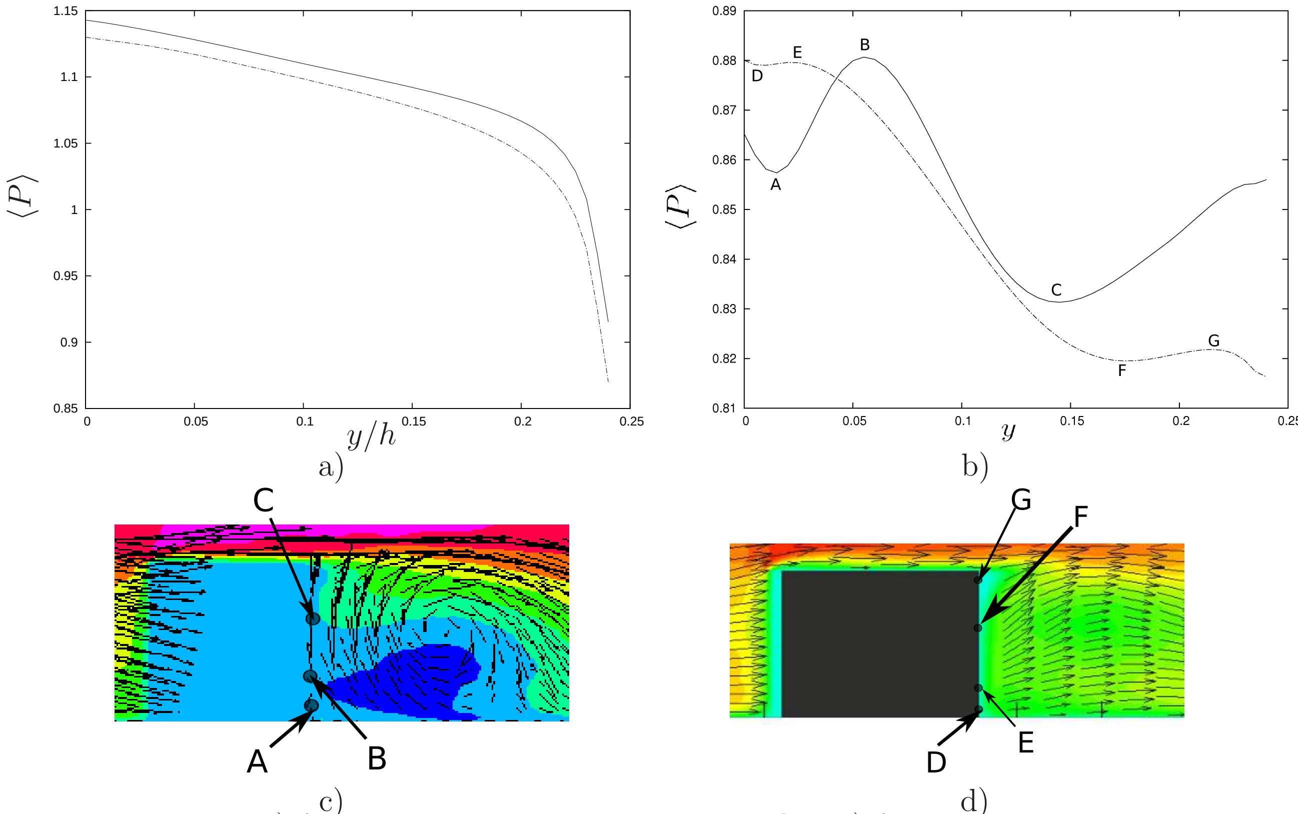

Figure 4–13: a) Averaged rib upstream pressure profile. b) Averaged rib downstream pressure profile: —·— segmented V-shape; —— , continuous V-shape (Data from Toro [33]), c) Continuous V-shape time averaged streamwise velocity close-up on one rib with marked inflection points, d) Segmented V-shape time averaged streamwise velocity close-up on one rib with marked inflection points.

the frontal area is higher than that in the back of the rib causing a resultant force in the direction of the flow. This resultant force is known as the form drag. The form drag is given by integral of pressure projected onto the streamwise direction: $\bar{P}_d = \lambda^{-1} \int \langle P \rangle \overrightarrow{\mathbf{n}} \cdot \overrightarrow{x} ds$ where $\overrightarrow{n}$ is the surface normal to the wall and ds is the coordinate that prescribes the wall surface. Figure 4–13a and 4–13b show plots of the time and space average upstream and downstream wall pressure distribution. Refer to figure 4–14 for a schematic of the rib where each wall is identified. The upstream pressure distribution is similar for both configurations. On both cases the maximum pressure is located at the bottom of the cavity and the minimum is located at the crest plane. It is observed that the pressure decays linearly up to a distance of $.05h$ from the crest plane. Then the pressure decays abruptly. A similar trend was observed for square bars ribs by Leonardi et. al. [24]. The linear drop in pressure is caused by the redistribution of the fluid particles in the spanwise direction and the sudden drop is due to the transition from a high pressure zone inside the cavity to the pressure at the crest plane. The segmented and continuous V-shape ribs upstream pressure follow a similar trend but is approximately 1.65 percent more for the continuous V-shaped ribs.

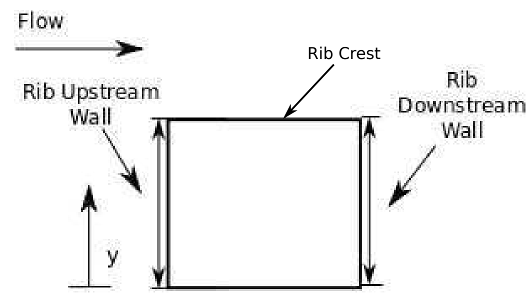

Figure 4–14: Rib Surfaces Schematic

The averaged pressure profile on the downstream wall is shown in figure 4–13b. There are two local minimum (A and C) and one maximum (B) in the pressure profile of continuous V-shaped ribs. The first local minimum is found at $y = 0.0125h$ (A). Then the pressure reaches a peak at $y = 0.0625h$ (B) and drops again. The pressure minimum is located at at $y = 0.15h$ (C). The pressure rises at a constant rate from y=0.15h to the crest plane. The inflection points for continuous v-shaped turbulators are marked on the rib in figure 4–13c. The inflections are related to the local velocities in the downstream wall. From point A to B, the pressure rises due to the reverse flow in that region. In fact, the lowest streamwise velocity is observed in the position where point B is located. Since the surface is pointing downstream, the higher pressure must be located where the velocity is at it lowest (backflow). Also, the velocity profile changes in the region bound to point C, causing another inflection point. For the segmented V-shaped ribs, there are two local maximum (E and G) and two local minimums (D and F). The first local pressure minimum is located at $y = 0.00625h$ (D). Then, the pressure rises and reaches a peak at

$y = 0.025h$ (E). After the peak, the pressure decreases at a constant rate until $y = 0.0175h$ (F). Finally the pressures rises to the local peak G and decreases until it reaches the crest plane. The inflection points for segmented v-shaped turbulators are marked on the rib in figure 4–13d. When compared with the continuous V-shaped average streamwise velocity at the same region, the recirculation is non-existent for the segmented V-shaped turbulators, which leads to a more uniform drop in pressure from the wall to the crest plane. Nevertheless, small changes in the streamwise velocity are observed in the region near to the inflection points. There are significance differences between each pressure profile. In both cases, the pressure drops from the wall to a distance inside the cavity. The difference is that, for continuous V-shaped ribs, the pressure drop is 0.75 and for the segmented V-shape ribs this pressure drop is 0.1. The same occurs for the first maximum. The pressure rises 2.25 from point A to B while the increase between D and E is 0.1. In addition, the locations of D and E are translated to the left, closer to the wall. There is a constant drop from the peaks E and B for each case but, the pressure minimum is located farther from the wall for the segmented V-shape rib configuration. This minimum (F) is lower than that from for continuous V-shape configurations (C). For the continuous V-shape ribs, the pressure rises after point C while, for the segmented V-shape ribs, the pressure rises up to a maxima G and then drops until it reaches the crest plane. The differences in the downstream wall pressure profile are mainly due to the differences in the flow structure inside the cavity. Toro [33] observed a strong average recirculation downstream of the rib turbulator which, in fact, causes the inflections points on the pressure profile on the downstream surface. On the other hand, for the segmented V-shape ribs, the flow entering from the gap weakens the recirculation behind the ribs (See Fig 4–12) and by consequence the pressure profile is different.

4.4.3 Total Drag

As expected, the form drag for segmented V-shaped turbulators is 13.7 percent lower than that for continuous ribs (Fig. 4–15). In fact, there is less area normal to the streamwise direction where the flow impinges. On the other hand, the frictional drag is 95 percent higher for the Segmented V-Shape configuration, due to the high speed streak in the gap between the turbulators. Since the form drag is the dominant component of the total drag, for $w/k = 3$ V-shaped roughness, the total drag ($C_f + P_d$) is 9.23 percent higher for the Non-segmented V-shape configuration. When compared to a flat channel the segmented and continuous V-shaped turbulators produce, respectively, 44 and 48 times more drag.

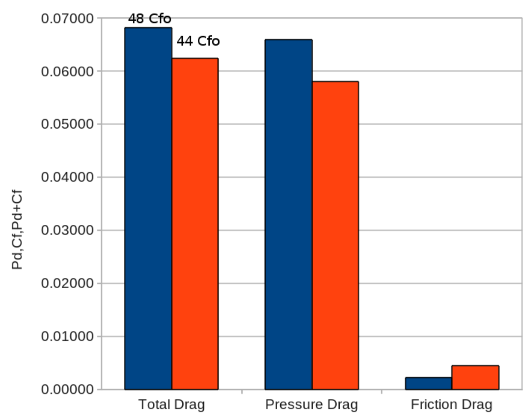

Figure 4–15: Frictional, form and total drag: blue; two ribbed walls, red; one ribbed wall. Cd_o is the flat channel drag.

4.5 MEAN TEMPERATURE

Figure 4–16 shows the temperature distribution averaged in time, spanwise and streamwise directions, for continuous ribbed V-shaped channels and segmented ribbed V-shaped channels. The mean temperature for a flat channel is shown as reference. The non-dimensional temperature boundary conditions prescribed are $T = 1$ for the bottom wall and $T = -1$ for the top wall. The bottom and top wall correspond to a hot and cold wall respectively. In addition, the turbulators located at the bottom wall have an uniform temperature of $T = 1$ while the turbulators at the top wall have a uniform temperature of $T = -1$.

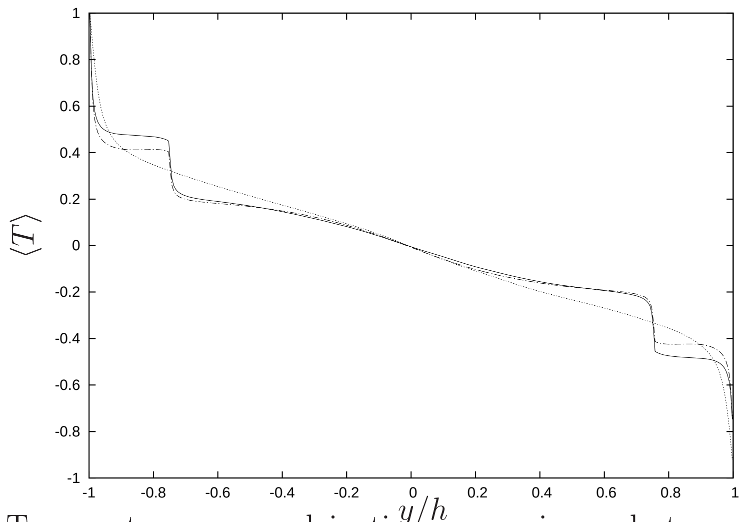

Figure 4–16: Temperature averaged in time, spanwise and streamwise direction: —·— , segmented V-shape; —— , continuous V-shape (Data from Toro [33]); ········ , Flat Channel.

For both cases, there is a high temperature gradient at the wall and the crest plane. The gradient at the wall is higher for the segmented V-shaped ribbed channels. This means that conduction is higher near the wall for segmented V-shaped turbulators. In fact, this is due to the changes in the flow structure caused by the gap of the turbulator; it weakens the spanwise recirculation and increases the overall flow momentum inside the cavity, and by consequence more heat is removed from the normal wall. On the contrary, the gradient of temperature at the crest plane is higher for the continuous V-shaped ribbed channel. Since these differences are almost equal, the linear temperature distribution at the center of the channel remains approximately the same for both configurations. The temperature gradient at the wall for the segmented and continuous V-shaped is larger than that for a flat channel.

4.6 TEMPERATURE FLUCTUATIONS

Figure 4–17 show the temperature RMS across the normal direction for continuous ribbed V-shaped channels and segmented ribbed V-shaped channels. The flat wall temperature fluctuations are shown as a reference. As expected, the fluctuations are low in the center of the channel due to low temperature gradient. On the contrary, there are high fluctuations inside the cavity for both cases. The segmented V-shaped turbulator configuration has the highest temperature fluctuation, similarly to what happens for turbulence intensity. The higher level of fluctuations agrees qualitatively with the increased heat transfer discussed in the temperature profile.

As expected, the temperature fluctuations in the wall are higher for a V-shaped channel when compared to that in a flat channel. Fluctuating temperatures are similar in the center of the flat and V-shaped channel. This is due, as discussed earlier, to the reduction of secondary motions in the center of the V-shaped channel, resulting in similar fluctuations a as flat channel.

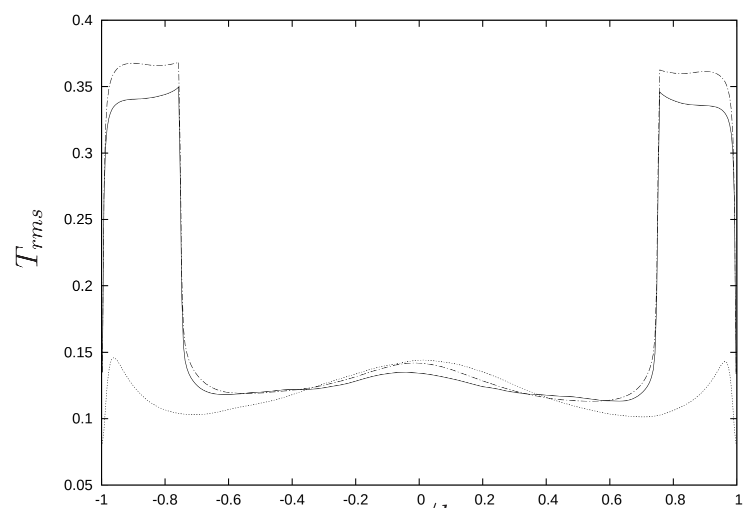

Figure 4–17: Temperature fluctuation statistics in time, spanwise and streamwise direction: —·— , segmented V-shape; —— , continuous V-shape (Data from Toro [33]); ······· , Flat Channel.

4.7 HEAT TRANSFER

4.7.1 Turbulent Heat Flux

Figure 4–18 shows the turbulent heat flux $\langle Tv \rangle$ averaged in time, spanwise and streamwise direction, for continuous ribbed V-shaped channels and segmented ribbed V-shaped channels. The heat flux of a flat channel is shown as reference. Results show that the averaged turbulent heat flux is slightly higher (9 percent more) for the segmented V-shaped ribbed channel. This increment of turbulent heat flux occurs inside the crest plane region. At the crest plane and on the center region of the channel, the difference between the turbulent heat flux does not change. This means that the key element on enhancing the heat transfer lies inside the cavities. In fact, the turbulent intensity $\langle u'u' \rangle$ (Fig 4–9a) and temperature fluctuations $\langle T' \rangle$ (Fig. 4–17) in the cavity is higher for the segmented V-shaped turbulators, hence there is more mixing between the inner channel and the rough wall. When compared to a flat channel, the heat transfer augmentation of a segmented and continuous V-shaped channel is 7.32 and 6.75 times larger respectively.

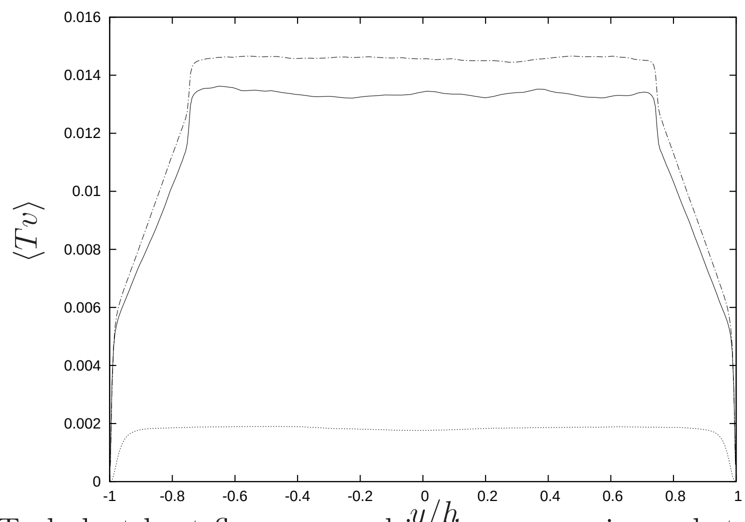

Figure 4–18: Turbulent heat flux averaged in time, spanwise and streamwise direction: —·— , segmented V-shape; —— , continuous V-shape; ········ , Flat Channel.

4.7.2 Wall heat flux

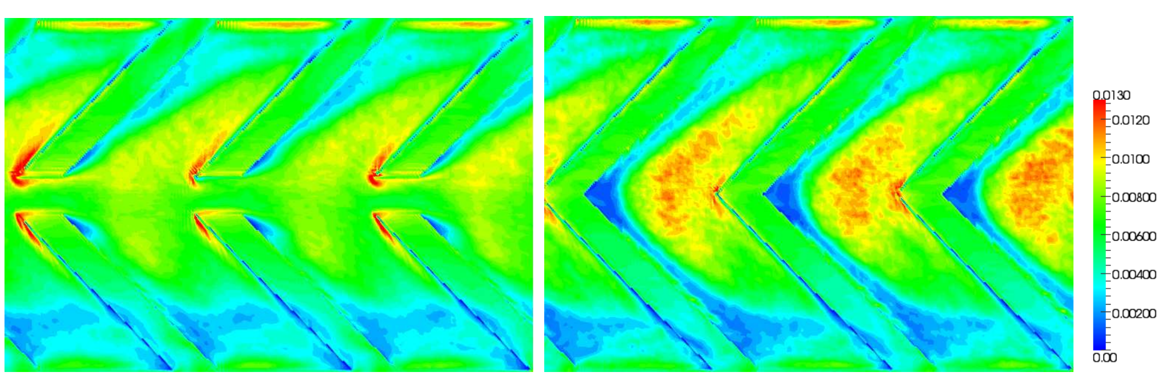

a) b)

Figure 4–19: Heat flux at the wall: a) Segmented V-shaped and b) Continuous V-shaped (Data from Toro [33])

Using the non-dimensional energy equation, the steady-state heat flux at the wall is given by:

$$\langle q''_w \rangle = \frac{\partial \langle T \rangle}{\partial y} \frac{1}{RePr}|_{y=0} \tag{4.2}$$

at y=0.

Higher heat transfer is observed near the turbulator gap, near the side walls and where there is flow entering into the cavity from the normal direction (Fig. 4–19a). High heat flux peaks are observed inside the cavity for the continuous V-shaped turbulators configuration (Fig. 4–19b). On the other hand, there is a drop of heat flux downstream of the turbulator, due to the flow recirculation. In fact, the gap of the segmented V-shaped turbulator reduces the flow recirculation, therefore the drop of local heat flux is lower (See Figure 4–19a). This is one reason of why the segmented V-shaped configuration promotes more heat transfer than the continuous V-shaped configuration. Also the increment of turbulence levels and temperature fluctuations in the cavity leads to an increase in heat transfer for the segmented V-shaped turbulators. The heat flux peaks are higher for the continuous V-shaped but the heat flux drop found downstream the turbulators causes a reduction on the overall heat transfer.

4.8 TIME CONVERGENCE

Figure 4–20a shows a plot of the channel averaged pressure gradient for each timestep. The pressure gradient is oscillating between values of -0.052 and -0.065 which means that the numerical simulations have reached momentum steady-state. The oscillation is due to the nature of turbulence. Figure 4–20b shows space averaged temperature for two different positions on the normal direction. The temperature is oscillating on both positions and is consistent with the boundary conditions. The system has reached thermal steady state to a good approximation.

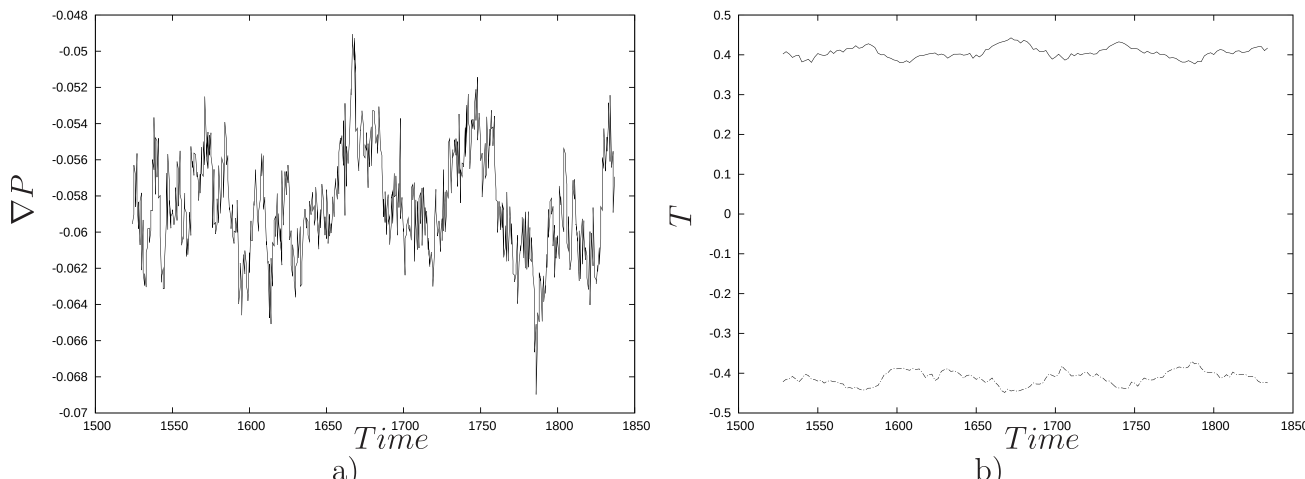

Figure 4–20: Time history of the mean pressure gradient (a) and temperature in two points of the domain (b).

CHAPTER 5
ONE WALL CONTINOUS V-SHAPE CONFIGURATION

5.1 FLOW CONFIGURATION

The flow configuration is the same as that of V-shaped turbulators (See fig. 5–1. However, in this case turbulators are placed on one-wall only. The temperature on the lower walls is $T = 1$ while on the upper wall is $T = -1$. Therefore heat is transported away from the lower wall and dissipated on the upper wall. The Reynolds number $Re = \frac{U_c h}{\nu}$ is 10400, while the Prandtl number Pr is set equal to 1; here, U_c is the centerline velocity and ν is the kinematic viscosity, h the channel half height. The computational box is $6h \times 2h \times 2h$ in x (streamwise), y (wall-normal) and z (spanwise direction) respectively. Periodic boundary conditions apply in the streamwise and spanwise direction. In the vertical direction a non uniform grid was used with 192 grid nodes. Mesh sizes in the other two directions are uniform with 192 points in spanwise direction and 640 in streamwise direction, yielding typically about 24 million nodes within the domain.

5.2 FLOW STRUCTURE

The flow structure inside the cavity is similar to that corresponding to turbulators on both walls (Fig. 5–2). The velocity of the flow crossing the crest plane into the cavity is greater when turbulators are on both the walls. As a consequence, ejections are more intense. Since there are no turbulators on the upper wall, there will be a lower mixing between the upper flow and the ribbed wall which it will lead to a heat transfer and form drag reduction.

a)

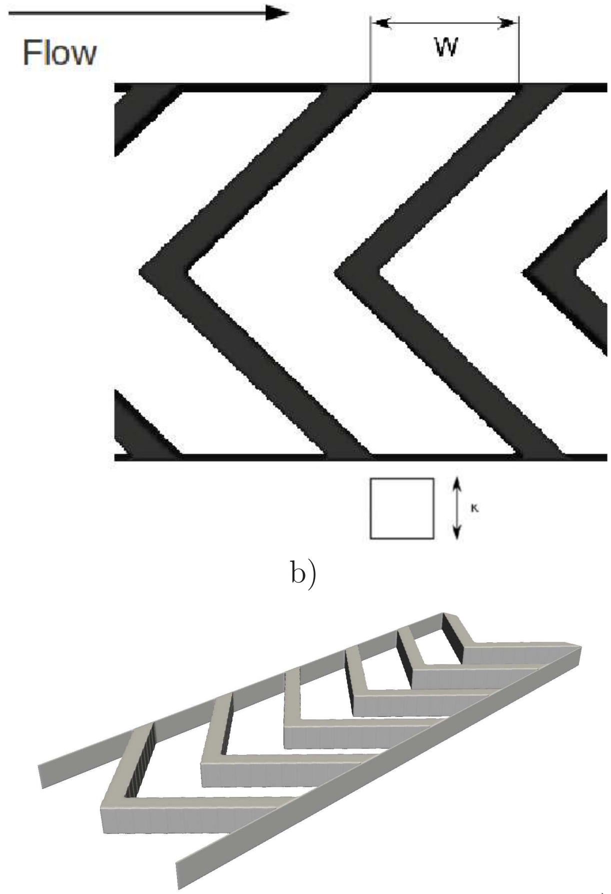

b)

Figure 5–1: a) One Wall V-Shaped geometrical configuration. b) Three dimensional view of the flow configuration

5.3 FLOW STATISTICS

The streamwise velocity averaged in time, spanwise and streamwise direction is shown in figure 5–3. For the configuration with turbulators on one wall only, the maximum streamwise velocity is shifted upward from the center of the channel to approximately $0.3h$ from the top wall. This is due to the different drag on the flat and rough wall as discussed in Leonardi et al. [24]. The streamwise velocity of the flat channel is higher than that for the one wall V-shaped channel from the roughened wall up to $y = 0$. On the contrary, the velocity peak of the one wall V-shaped channel is larger in the region near to the flat wall. This is because the drag of the rough wall is higher than that over a smooth wall. Also the mean velocity gradient on the flat wall is greater for the one-wall V-shaped channel when compared

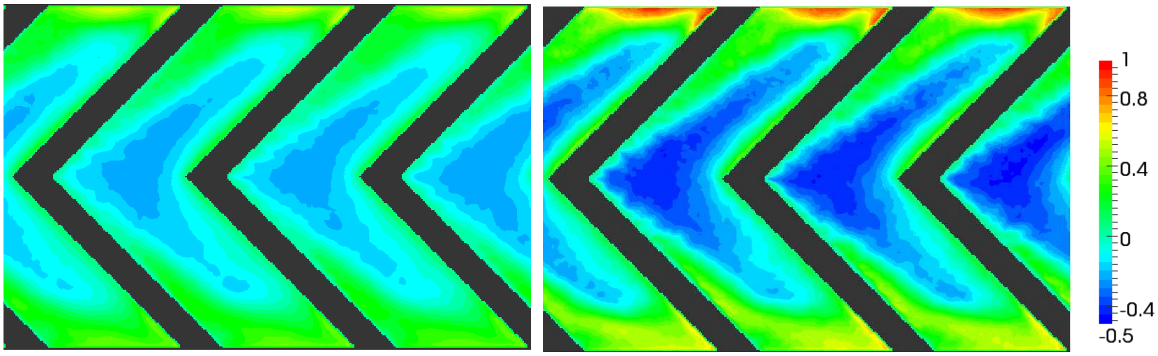

a) b)

Figure 5–2: Time averaged normal–wall velocity color contours. a) turbulators on one wall only and b) on both walls (Data from Toro [33]).

with that of a flat channel. By consequence, the friction drag of the flat wall of the V-shaped channel is higher.

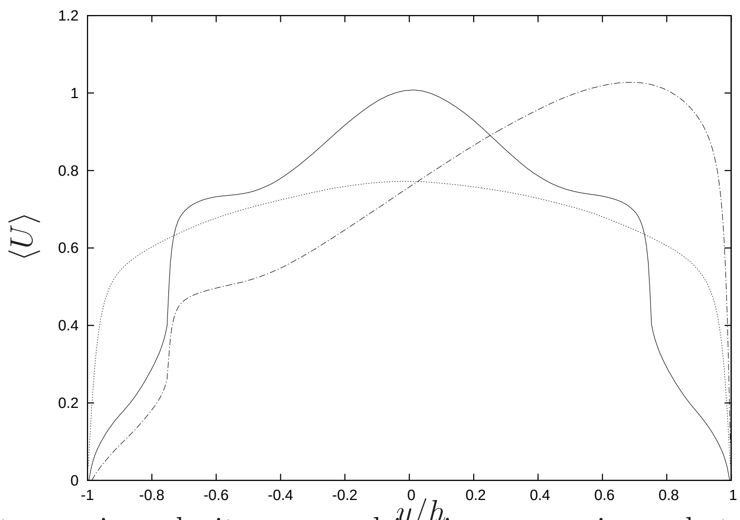

Figure 5–3: Streamwise velocity averaged in time, spanwise and streamwise direction: —·— , one wall V-shaped;—— , both walls V-shaped (Data from Toro [33]); ········ , Flat Channel.

Figure 5–4 shows the streamwise velocity turbulent intensity along the normal direction for one wall ribbed V-shaped and both walls ribbed V-shaped channels. Results show that the streamwise turbulent intensity is higher at every location when V-shaped turbulators are on both the walls. For the rough wall, the turbulent intensity have the same trend for both configurations. In fact, the difference lies on the turbulent intensity magnitude. Results shows that the turbulent intensity trend is different for $y > 0$. When V-shaped turbulators are on both walls, the streamwise

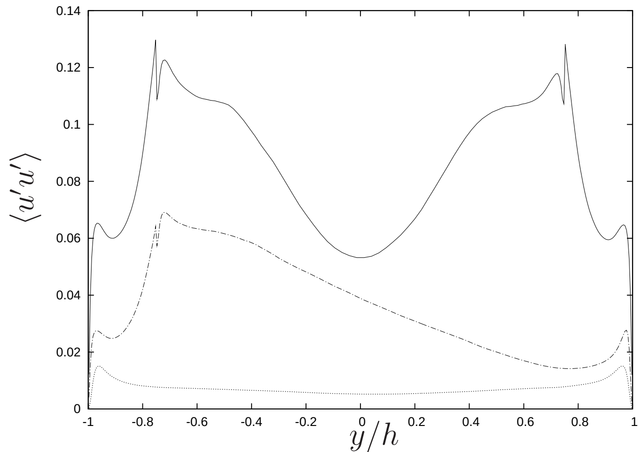

a) b)

Figure 5–4: a) Streamwise velocity turbulent intensity statistics in time, spanwise and streamwise direction: —·— , one wall V-shaped;—— , both walls V-shaped (Data from Toro [33]); ········ , Flat Channel.

turbulence intensity is symmetric about the normal direction. On the contrary, when V-shaped turbulators are placed on one wall, the streamwise turbulence intensity decreases from the crest plane until it reaches a minimum at about $1k$ of the flat wall. To a close approximation, the minimum of turbulent intensity magnitude corresponds to the maximum streamwise velocity.

The streamwise velocity turbulent intensity is larger for all $y's$ for the one wall V-shaped channel when compared to that in a flat channel. As explained in Chapter 4, this is because of the secondary flows and sidewalls ejections caused by the V-shape geometry. Also, the turbulent intensity is higher in the flat wall of the one-wall V-shaped channels because the mean streamwise velocity gradient is higher than that in a flat channel. The increase of turbulent intensity due to a one-wall V-shaped channel is less than the increase caused by the both-walls V-shaped channel.

5.4 DRAG

5.4.1 Form Drag

As explained in the previous chapter, the form drag is directly related with the pressure exerted on the roughness surfaces. Pressure profiles for the upstream and downstream walls are shown in figure 5–5a and 5–5b respectively. For the upstream pressure profile (fig 5–5a), the pressure is higher for the both walls ribbed channel except for $y > 0.23h$. The pressure is higher when turbulators are placed on both walls due to the redistribution of the flow in the y direction when only one wall is roughened. This redistribution causes a reduction in the momentum of the flow near the rough wall and, by consequence, the stagnation pressure reduces. In fact, Tanda [32] observed that, for 45 angled square ribs, the ratio of the friction factors (f/f_o) is about three times higher as compared with one-wall ribbed channels. The redistribution of the flow is what causes this decrease in the drag and the effect is observed in the pressure profile. On the downstream wall (Fig. 5–5b), the pressure profiles relative to the case with turbulators on both walls is similar to that with turbulators on one wall only. But, the pressure is ten percent higher for the one-wall ribbed channel. Also, the flow redistribution is the cause for the increase in the pressure of the rib downstream wall.

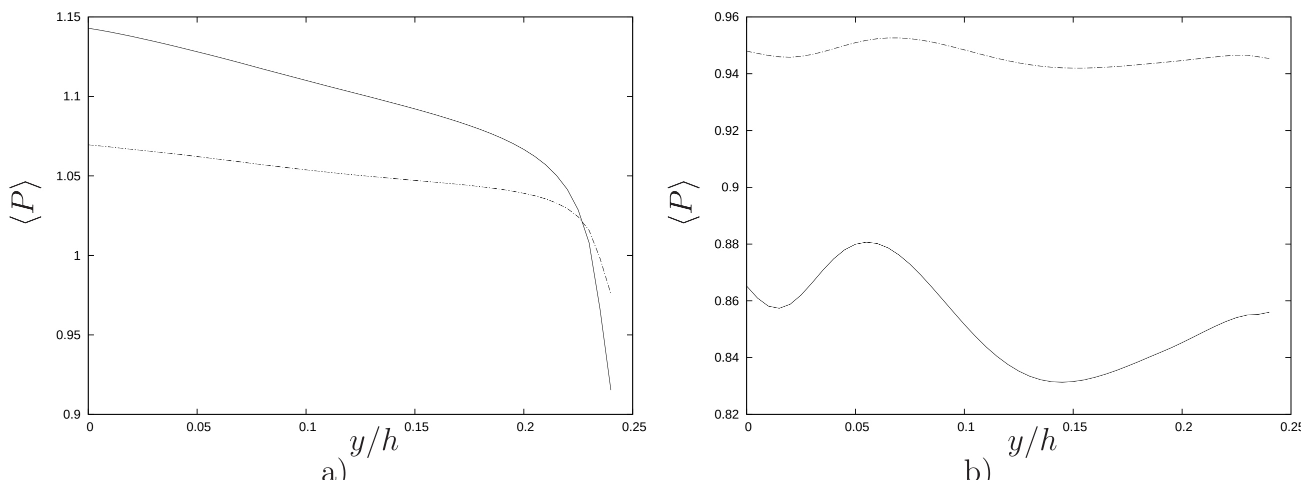

Figure 5–5: a) Averaged rib upstream pressure profile. b) Averaged rib downstream pressure profile: —·— V-shape on one-wall ; —— , V-shape on both walls (Data from Toro [33]).

The higher pressure on the ribs when turbulators when turbulators are on two walls is not surprising. In fact, the flow velocity above the roughness is higher, and pressure should scale with the dynamic pressure ρV^2, where V is the velocity in the outer layer. Since here we are in a channel, it is not clear where the outer layer

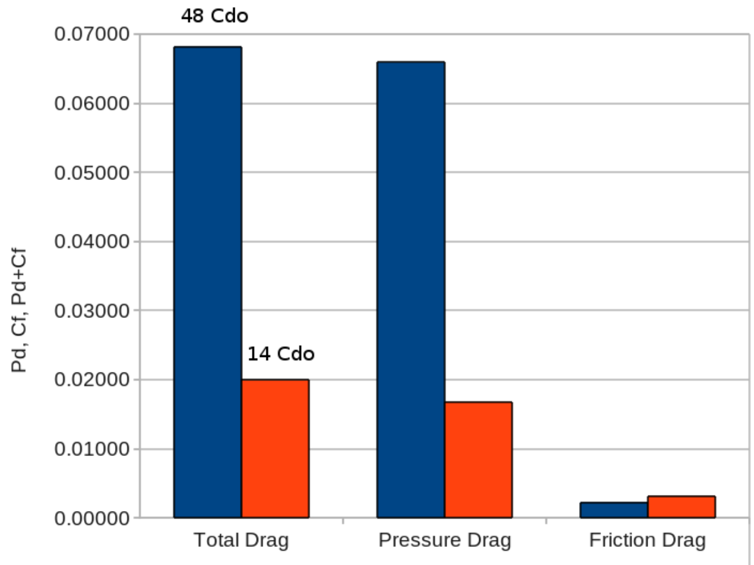

Figure 5–6: Frictional, form and total drag: blue two ribbed walls, red one ribbed wall. Cd_o is the flat channel drag.

starts. However we found that scaling the form drag by the flow velocity 0.05 above the crest plane, $C_d = \frac{\int_0^k (\langle P_u \rangle - \langle P_d \rangle) dy}{(1/2 \rho U^2 k)}$ (where P_u is the pressure on the upstream face, P_d on downstream face and V is the velocity $0.05h$ above the crests) is 1.03 for V-shaped turbulators on both walls and 0.94 when turbulators are on one wall only. So the increase of a factor of 3 of the form drag does not depend on a different flow structure, but rather on different momentum of the flow impinging the roughness elements. This is in qualitative agreement with Leonardi et. al. [28] who found that the roughness function for transverse square bars does not depend whether turbulators are on both walls or one wall only.

5.4.2 Total Drag

The drag relative to the configuration with turbulators on both the wall is 3.42 times higher than that corresponding to turbulators on one-wall only (Fig. 5–6). The mayor reduction in drag is mainly due to the lack of form drag of the top wall, the elimination of the top wall streamwise large scale vortex formed by the ejection and the redistribution of the flow towards the top wall. Perhaps one would expect the drag for 2 ribbed walls being twice as much that with one ribbed wall. However, when the ribs are placed on the wall, the cross section of the channel is reduced

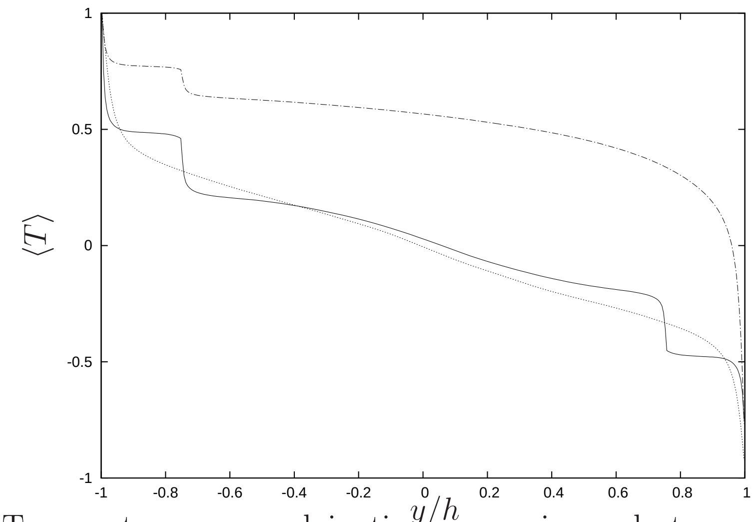

Figure 5–7: Temperature averaged in time, spanwise and streamwise direction: —·— , one-wall V-shaped; —— , both walls V-shaped (Data from Toro [33]); ········ , Flat Channel.

thus increasing the mean velocity (V). Since the momentum is larger when ribs are on both walls, despite the drag coefficient of the single obstacle remains the same (c_d), the total drag $(\rho V^2 c_d S)$ increases. Moreover, the friction drag is 1.39 higher for the one-wall V-shape configuration due to the flat wall. When compared to a flat channel, the drag of the one-wall V-shaped channel is 14 times higher.

5.5 MEAN TEMPERATURE

Figure 5–7 shows the averaged temperature distribution across the normal direction for both configurations (one ribbed wall and both ribbed walls). The mean temperature relative to the flat channel is shown as reference. The temperature gradient at the rough wall is higher when turbulators are placed on both the walls. Inside the cavity $(\pm 1 < y < \pm 0.75)$ the temperature remains almost constant and at the crest plane, the temperature gradient is larger when both walls are ribbed. For the channel with one ribbed wall only, the upward shift of the mass in the channel, determines higher velocity and temperature gradients at the upper wall than those corresponding to a flat channel. Results also show that the mean temperature gradient at the wall is higher than that for a flat channel. This is due to the increased heat transfer at the rough wall.

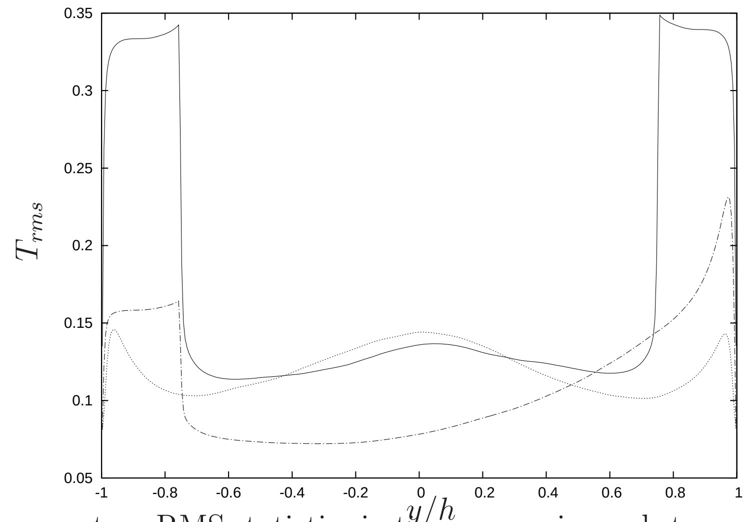

Figure 5–8: Temperature RMS statistics in time, spanwise and streamwise direction: —·— , one-wall V-shaped; —— , both walls V-shaped (Data from Toro [33]); ········ , Flat Channel.

5.6 TEMPERATURE FLUCTUATIONS

Figure 5–8 shows plots of the temperature RMS across the normal direction for the two configurations with one ribbed wall and both ribbed walls. The fluctuation are low in the center of the channel. The temperature fluctuation is higher when turbulators are placed on both walls except for $0.5h <= y <= 0.75h$. This is due to the fluctuations caused by the turbulent boundary layer on the flat wall.

As explained in Chapter 4, the temperature fluctuations are similar for the flat channel and V-shaped turbulators in the center ($-0.6 <= y <= 0.6$). On the contrary, differences are observed in the region near the wall due to the rough boundary conditions. For one-wall V-shaped turbulators, higher velocity gradients observed near the flat wall.

5.7 HEAT TRANSFER

The normal heat flux is composed of the turbulent heat flux and molecular conduction. Plots of the results for normal heat flux ($\langle vT\rangle + 1/(Re \cdot Pr)\partial\langle T\rangle/\partial y$) are shown on figure 5–9. The heat flux for both walls ribbed channels is approximately 3.04 more than one-wall ribbed channels. The result is expected because the V-shaped roughness promotes recirculation and a large scale streamwise vortex at the sidewalls. Since the roughness is removed from the upper wall, there is a reduction of flow mixing between outer region and near wall region, resulting in a decreased heat transport. The reduction of drag is the advantage of one-wall V-shaped ribbed channel. Results also show that the one-wall V-shaped turbulators produce a 2.31 heat transfer augmentation with respect to the flat channel.

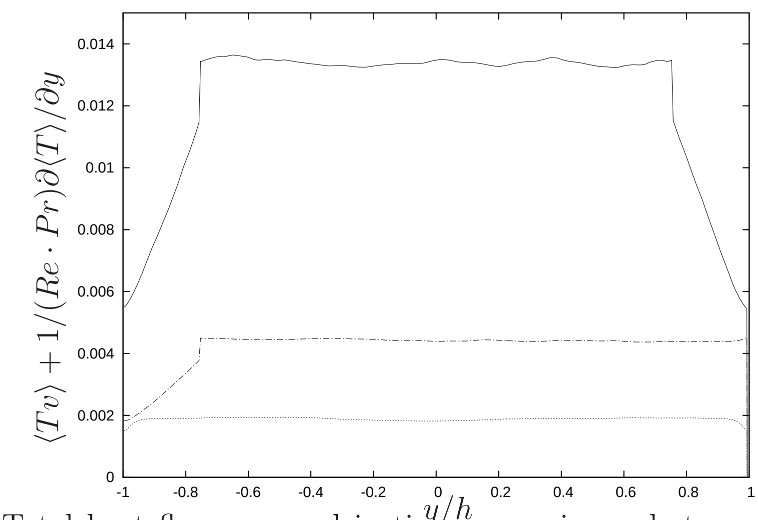

Figure 5–9: Total heat flux averaged in time, spanwise and streamwise direction: —·— , one-wall V-shape; —— , both walls V-shaped (Data from Toro [33]); ········ , Flat Channel.

5.7.1 TIME CONVERGENCE

Figure 5–10a shows a plot of the channel averaged pressure gradient for each timestep. The pressure gradient is oscillating between values of -0.012 and -0.019 which means that the numerical simulation have reached statistical steady-state. The oscillation is due to the nature of turbulence and the large scale vortices which render over the rough wall. Figure 5–10b show plots of the space averaged temperature for two different positions on the normal direction. The temperature is oscillating on both positions and is consistent with the boundary conditions and temperature distribution (Figure 5–7). The system has reached thermal steady state to a good approximation.

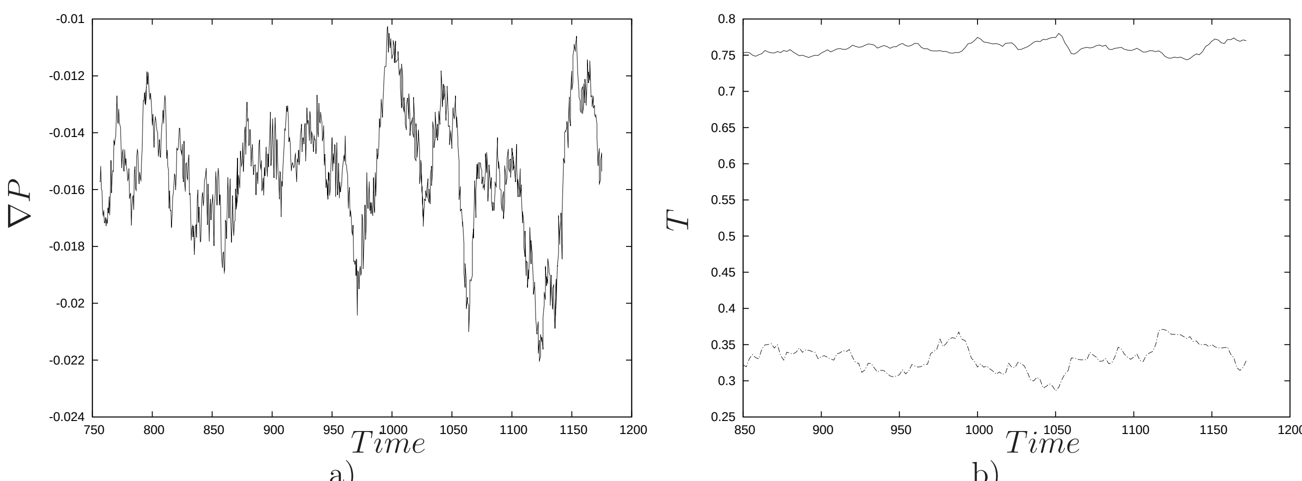

Figure 5–10: Time history of the mean pressure gradient (a) and temperature in two points of the domain (b).

CHAPTER 6
$W/K = 5$ INCLINED AND V-SHAPED TURBULATORS WITH DIFFERENT ANGLES

6.1 FLOW CONFIGURATION

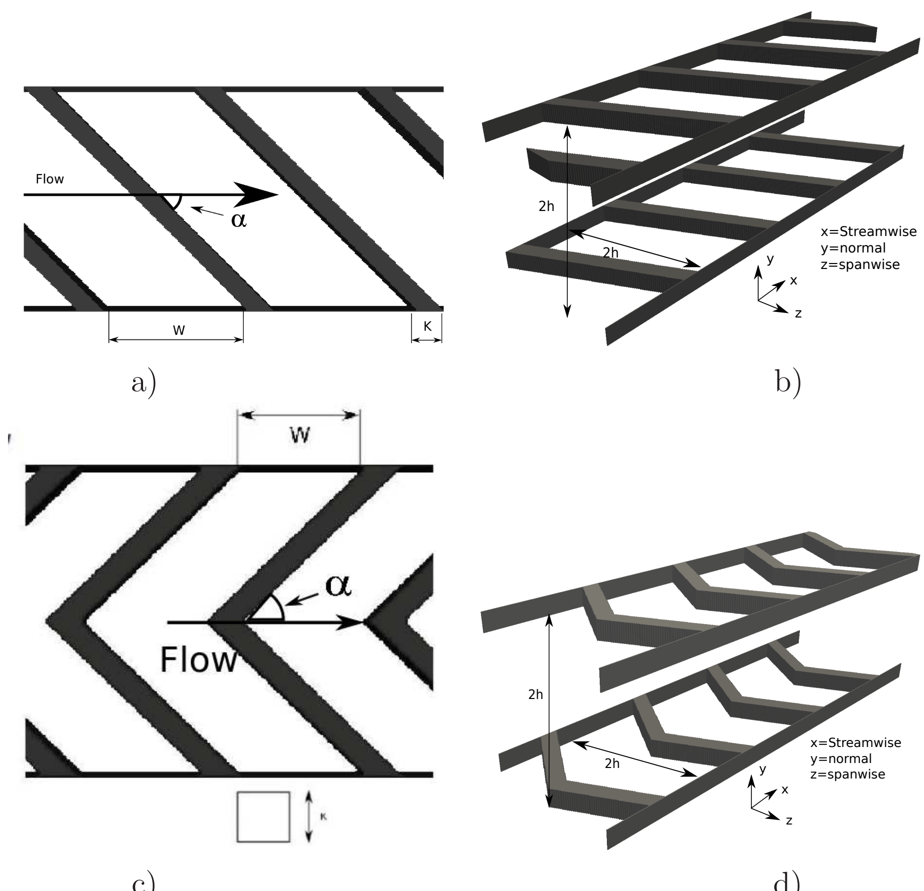

Figure 6–1: a) Inclined ribs geometrical configuration. b) Three dimensional view of the inclined flow configuration. c) V-shaped ribs geometrical configuration. d) Three dimensional view of the V-shaped flow configuration.

The flow configuration consist of rib turbulators placed on both walls. Two types of turbulators were considered: Inclined ribs (Fig 6–1a,b) which are made of straight ribs inclined with respect to the flow direction, and V-shaped ribs (Fig

6–1c,d) which are made of two separate straight ribs inclined with respect to the flow direction. Each rib is inclined by an angle α with respect to the flow direction as depicted in Fig 6–1a,c. Different angles are considered for each configuration: $\alpha = 45, 60$ degrees for the inclined ribs and $\alpha = 45, 60, 75$ degrees for the V-shaped ribs. The height of the ribs is $k/h = 0.25$ and the pitch over height ratio is $w/k = 5$, where k, h and w indicate for rib height, channel half height and pitch respectively. The non dimensional temperature boundary conditions for the lower walls is $T = 1$ while on the upper wall is $T = -1$. Therefore heat is transported away from the lower wall and dissipated on the upper wall. The Reynolds number $Re = \frac{U_c h}{\nu}$ is 10400, while the Prandtl number Pr is set equal to 1; here, U_c is the centerline velocity and ν is the kinematic viscosity, h the channel half height. The computational box is $6hx2hx2h$ in z (streamwise), y (wall-normal) and x (spanwise direction) respectively. Periodic boundary conditions apply in the streamwise and spanwise direction. In the vertical direction a non uniform grid was used with 192 grid nodes. Mesh sizes in the other two directions are uniform for both, the inclined and V-shaped ribs, with 192 points in spanwise direction and 482 (Inclined ribs) or 640 (V-shaped ribs) in streamwise direction.

6.2 FLOW STRUCTURE

The fields are statistical averaged in time for each variable.

Color contours of the normal-wall velocity in a horizontal section at the crest plane are shown in Figure 6–2. When the turbulators are inclined (Fig 6–2 a,b), the flows enters into the cavity and a stream follows the angle of inclination of the roughness geometry. Since the inclined geometry is not symmetrical in the spanwise direction, the secondary flow spanwise velocity will be in one direction and the flow will eject when the stream reaches the sidewall. On the other hand, two streams are formed inside the cavity of a V-shaped turbulator. The particles in the cavity follows in good approximation the angle of the rib when this is 45 degrees. However, when

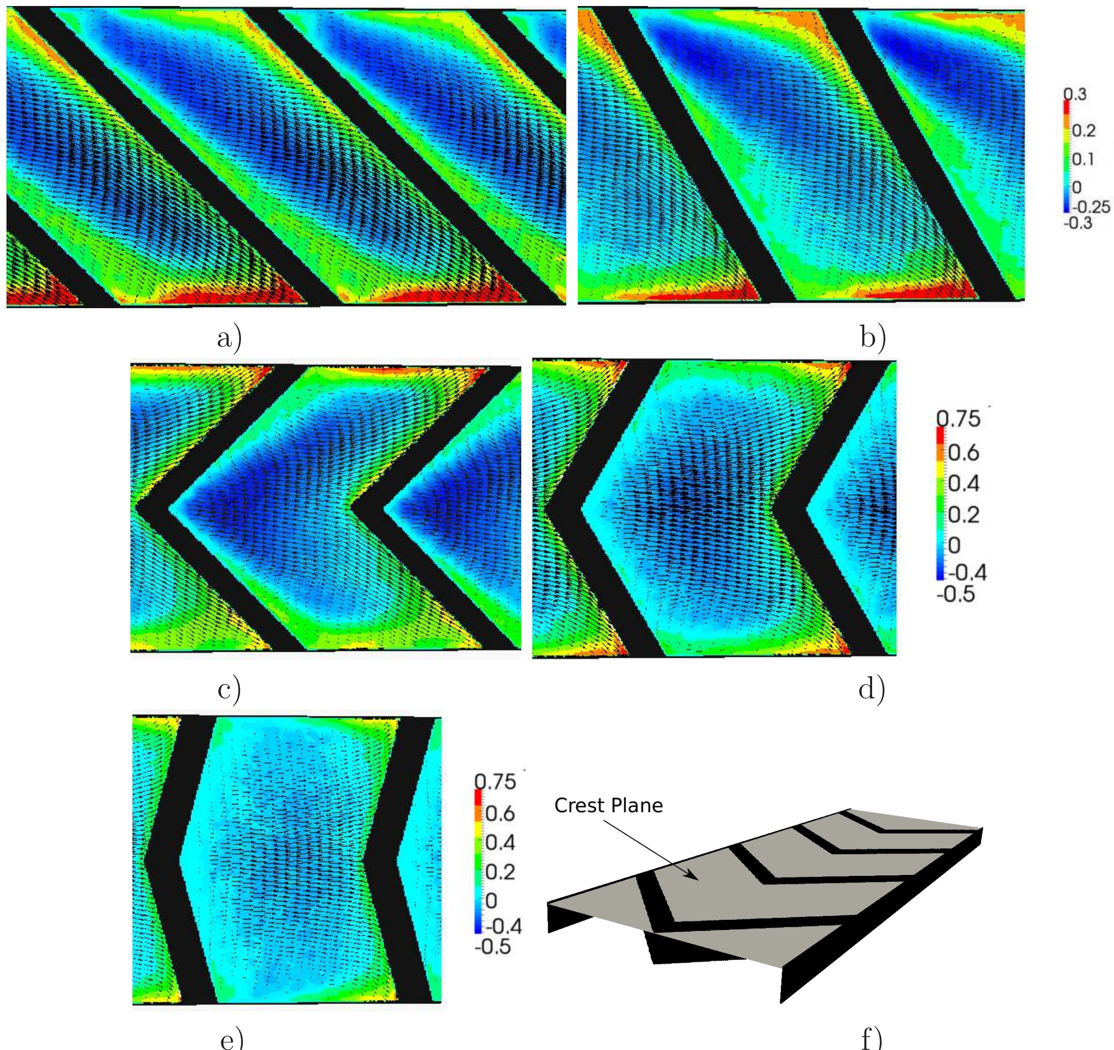

Figure 6–2: Color contours of normal wall velocity averaged in time and streamwise direction for a) Inclined $\alpha = 45$ b) Inclined $\alpha = 60$, c) V-shaped $\alpha = 45$ (Data from Toro [33]), d) V-shaped $\alpha = 60$ e) V-shaped V-shaped $\alpha = 75$, f) The crest plane.

the angle is increased, the velocity direction is closer to the mean flow direction. In fact, the extreme of 90 degree of inclination is a transverse square bar, which does not present a secondary spanwise motion (Leonardi et al. [24]).

The flow structure inside the cavity depends on the angle α. For the inclined ribs, the flow injecting the cavity is more intense for $\alpha = 60$ but the spanwise velocity is reduced due to the increase in the angle with respect to the flow direction. For the V-shaped ribs, the ejections are more intense when $\alpha = 45$. In fact, the V-shaped flow configuration induce more sidewalls ejections, when compared with the inclined ribs. With the increase of the angle α, ejections become weaker and the flow spanwise secondary motion is reduced.

6.3 FLOW STATISTICS

Figure 6–3 shows a plot of the time averaged streamwise velocity profiles along the normal direction for all flow configurations. A steep streamwise velocity ($\langle U \rangle$) gradient is present at $y = \pm 0.75$ for all configurations due to the transition from the roughened wall to the inner channel. The average streamwise velocity $\langle U \rangle$ inside the cavity decreases as the angle α increases for both flow configurations. When the angle α is increased, the downstream wall prevents the flow to move towards the streamwise direction due to the non-slip condition prescribed at the wall and because the wall is impermeable.

Previous research has demonstrated that a rough wall has an effect in the boundary layer profile and, by consequence the velocity profile in the channel inner channel will be different when compared with a flat channel. The boundary layer is different for inclined and V-shaped ribs and changes with the inclination angle with respect to the flow. As shown in Fig 6–2, the flow structure in the cavity depends on the roughness geometry. The differences in the flow structure leads to different roughness functions in the logarithmic region and it will lead to shifts of the mean streamwise velocity in the inner channel. The velocity gradient at the crest plane is lower for inclined ribs. Since the flow rate is the same for all cases, the inclined ribs streamwise velocity is higher at the center of the channel when compared to that in V-shaped ribs. Also, due to the conservation of mass, the streamwise velocity at $\alpha = 60$ is larger to that in $\alpha = 45$ inclined ribs.

For the V-shaped ribs, the increase in the angle α has the effect of increasing the reverse flow from the wall up to $\Delta y = 0.1$ from the wall. The negative velocity inside the cavity is an indication that recirculation downstream each rib is stronger as the angle α increases. As the flow configuration approaches $\alpha = 90$, the separation

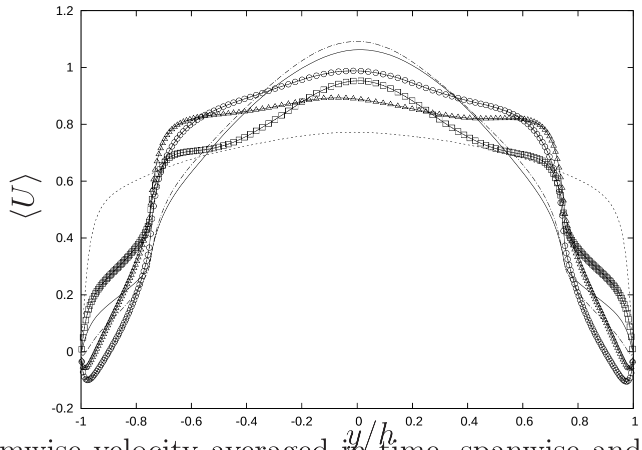

Figure 6–3: Streamwise velocity averaged in time, spanwise and streamwise direction: —— , Inclined $\alpha = 45$; —·— Inclined $\alpha = 60$; —— □ —— V-shaped $\alpha = 45$ (Data from Toro [33]); —— △ —— V-shaped $\alpha = 60$; —— ○ —— V-shaped $\alpha = 75$; ········ , Flat Channel.

downstream the rib will become stronger and the sidewall ejections will be weaker. In fact, for ribs with an $\alpha = 90$, the interaction between the flow inside the cavity and the inner channel is due to spanwise recirculation (see Leonardi et al. [24],[28]).

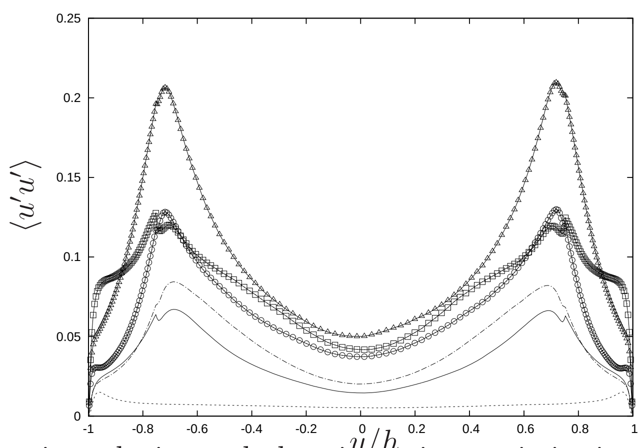

Figure 6–4: Streamwise velocity turbulent intensity statistics in time, spanwise and streamwise direction:—— , Inclined $\alpha = 45$; —·— Inclined $\alpha = 60$; —— □ —— V-shaped $\alpha = 45$ (Data from Toro [33]); —— △ —— V-shaped $\alpha = 60$; —— ○ —— V-shaped $\alpha = 75$; ········ , Flat Channel.

Figure 6–4 shows the streamwise velocity turbulent intensity across the normal direction for the inclined and V-shaped turbulators. The turbulent intensity is higher for the V-shaped ribbed channel. For the inclined ribs, $\alpha = 60$ induces higher fluctuations. This indicates that there is more interaction between the flow ejecting from the cavity into the inner channel. A peak in the turbulence intensity is observed at the crest plane ($y = \pm 0.75$) due to fact that the streamwise velocity increases with the reduction of the channel cross sectional area at the location of the ribs. Inside the cavity, an increment of the turbulence intensity is expected due to the presence of reverse flow caused by the separation downstream each rib.

For the V-shaped flow configuration, the highest turbulence intensity occurs for $\alpha = 60$. The turbulent intensity peak is 0.20 for $\alpha = 60$. This indicates that there is strong spanwise recirculation inside the cavity for this angle of inclination. On the contrary, in the near wall region, the turbulence intensity increases more rapidly up to 0.075 for $\alpha = 45$. As observed in Figure 6–3 the streamwise velocity is also higher in the near wall region for $\alpha = 45$. This increases the generation of turbulent structures near the wall, hence the increase in the turbulent intensity. The turbulent intensity decreases for $\alpha = 75$ due to a reduction of the interaction between the flow inside the cavity and the inner channel.

6.4 DRAG

A plot of the total drag coefficient (The sum of the form drag and frictional drag, $P_d + C_f = F/(\rho U^2)$) for the inclined and V-shaped turbulators is shown in Fig 6–5 as a function of the angle α. In the inclined ribs configuration, the highest drag is found for $\alpha = 60$, 34 percent more than that calculated for ribs inclined at $\alpha = 45$. As described in section 6.2, there is a reduction of the average streamwise velocity inside the cavity and an increase in flow injection from the inner channel to the cavity. This combination will lead to an increase in the total drag.

The V-shaped turbulators experience a total drag higher than that for inclined ribs regardless of α. The flow structure is completely different; there is more interaction between the inner channel and the rough wall. The highest drag reported is found for $\alpha = 60$ and it is due to the recirculation behind the rib which induces large pressure gradients between the upstream and downstream faces of the obstacle. On the other hand, the drag decreases for $\alpha = 75$ and while the average streamwise

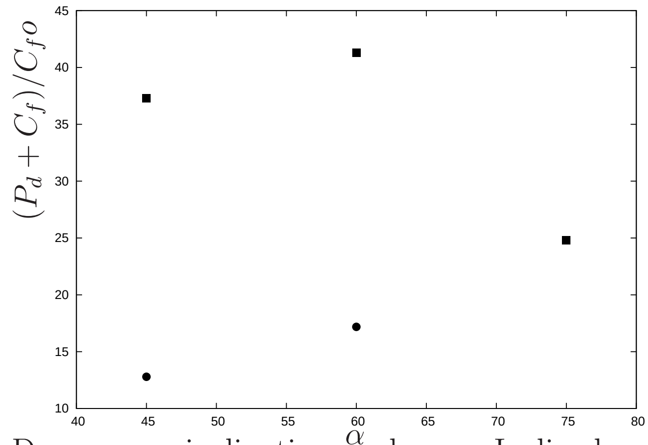

Figure 6–5: Total Drag versus inclination angle α: ● Inclined ; ■ V-shaped. $C_f o$ is the Flat channel drag.

velocity in the cavity is lower than that for $\alpha = 60$, the intensity of the ejections decreases greatly, which is the main mechanism of flow interaction between the cavity and the inner channel flow.

6.5 MEAN TEMPERATURE

Figure 6–6 shows the temperature distribution averaged in time, spanwise and streamwise directions, for all the turbulators. The non-dimensional temperature boundary conditions are $T = 1$ for the bottom wall and $T = -1$ for the top wall. The bottom and top wall correspond to a hot and cold wall respectively.

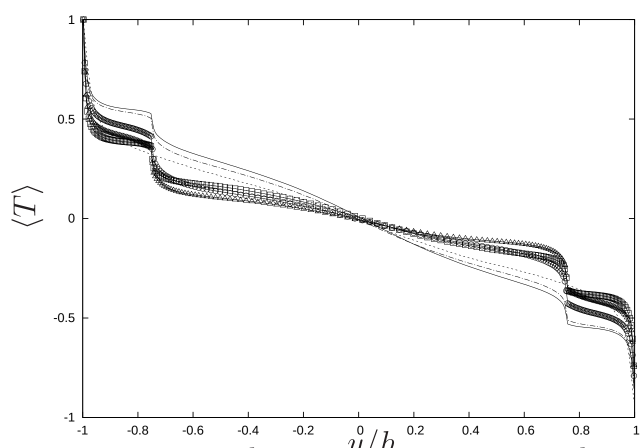

Figure 6–6: Temperature averaged in time, spanwise and streamwise direction: ——— , Inclined $\alpha = 45$; —·— Inclined $\alpha = 60$; ——— □ ——— V-shaped $\alpha = 45$ (Data from Toro [33]); ——— △ ——— V-shaped $\alpha = 60$; ——— ○ ——— V-shaped $\alpha = 75$; ········ , Flat Channel.

The overall temperature gradient is 30 percent higher for the V-shaped ribs when compared to the inclined ribs. For the inclined ribs an increment of 1.2 percent in the temperature gradient is observed for $\alpha = 60$ with respect to $\alpha = 45$. It has been observed previously that the mean temperature is related to the mean flow velocities and the turbulent intensities. In fact, the velocities are unknowns in the continuity and momentum equations and the temperature is the unknown of the energy equation, which is function of the velocities. Higher velocities and turbulent intensities are observed for $\alpha = 60$ and by consequence, temperature gradients at the wall is larger for this angle.

A similar trend is observed for the V-shaped ribs. The temperature gradients are larger for $\alpha = 60$, which is the configuration with the highest turbulent intensities at the crest plane. In fact, an increment in the flow interaction between the cavity and the inner channel increases the wall temperature gradients and enhances the heat transfer inside the turbulent channel.

6.6 TEMPERATURE FLUCTUATIONS

Figure 6–7 shows the temperature RMS along the wall normal direction for all the turbulators considered. As expected, the fluctuations are low in the center of the channel due to low temperature gradient at the centerline and the weak of secondary motions. On the contrary, there is an increment of the temperature fluctuations inside the cavity. Similar to the mean temperature profile, the fluctuations are greater for V-shaped turbulators and the inclined rib configuration. The highest fluctuating temperature is observed for $\alpha = 60$.

The maximum fluctuating temperature for the different V-shaped flow configurations are 0.307,0.338 and 0.353 for $\alpha = 75, 45, 60$ respectively. The high fluctuating temperature inside the cavity is due to the secondary motion induced by the turbulators. For example, cool air enters into the cavity and it is mixed with the hot air

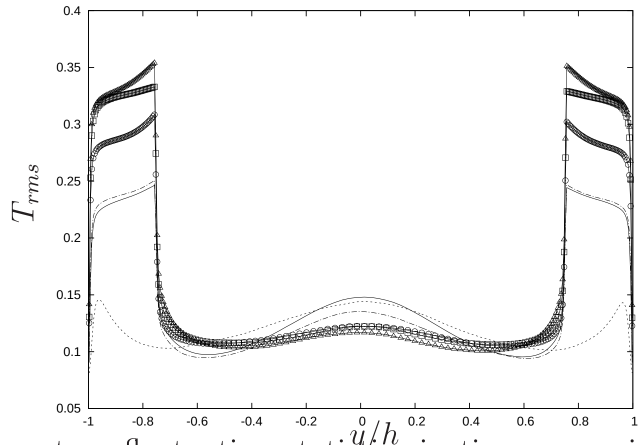

Figure 6–7: Temperature fluctuation statistics in time, spanwise and streamwise direction:—— , Inclined $\alpha = 45$; —·— Inclined $\alpha = 60$; —— □ —— V-shaped $\alpha = 45$ (Data from Toro [33]); —— △ —— V-shaped $\alpha = 60$; —— ○ —— V-shaped $\alpha = 75$; ········ , Flat Channel.

convected from the hot wall. Due to this process the temperatures inside the cavity will be different from the mean temperatures. Consistently with the turbulent intensity, the configuration with highest fluctuating temperatures is for $\alpha = 60$.

6.7 HEAT TRANSFER

The turbulent heat flux $\langle Tv \rangle$ averaged in time, spanwise and streamwise direction, is shown in Figure 6–8. V-shaped turbulators present a larger heat transfer than that measured over inclined ribs. For inclined ribs with $\alpha = 60$, the heat transfer is larger of about 6.6% than that for $\alpha = 45$. This increment is consistent with the difference between temperature gradients with respect to the normal direction and the level of temperature fluctuations inside the cavity.

For the V-shaped ribbed channel, the flow configuration with $\alpha = 60$ produced 5.8 percent more heat transfer when compared to that for $\alpha = 45$. On the contrary, for the flow configuration with $\alpha = 75$, the turbulent heat transfer is reduced of about 23% with respect to the configuration of $\alpha = 45$. In fact, the heat flux increase ($\alpha = 75$) or decrease ($\alpha = 60$) is consistent with the temperature fluctuations, where maximun fluctuations occurs for $\alpha = 60$.

Figure 6–9 shows a summary of the heat flux of each flow configuration. V-shaped turbulators are more effective in enhancing the heat transfer compared with

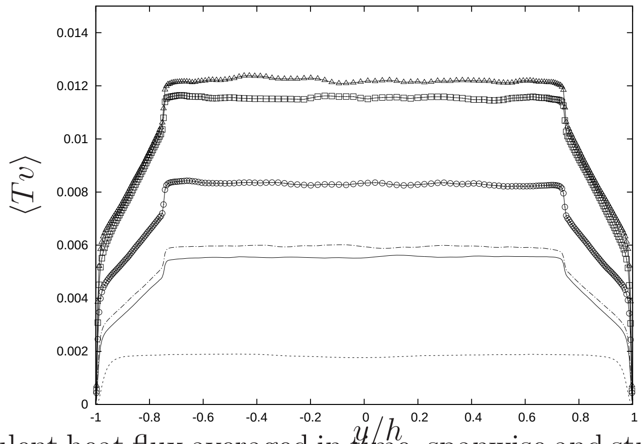

Figure 6–8: Turbulent heat flux averaged in time, spanwise and streamwise direction: —— , Inclined $\alpha = 45$; —·— Inclined $\alpha = 60$; —— □ —— V-shaped $\alpha = 45$; —— △ —— V-shaped $\alpha = 60$; —— ○ —— V-shaped $\alpha = 75$; ········ , Flat Channel.

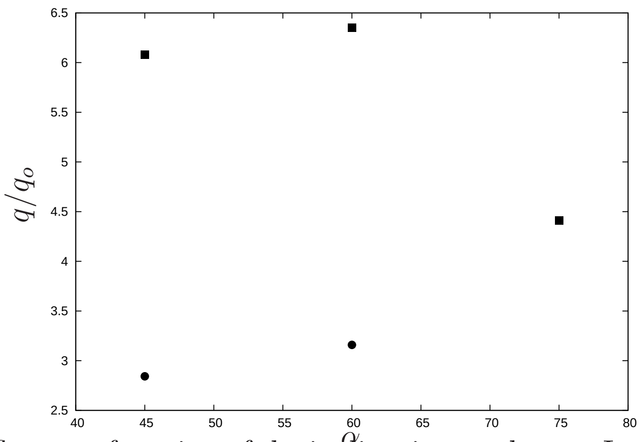

Figure 6–9: Heat flux as a function of the inclination angle α: ○ Inclined ; ■ V-shaped. q_o is the Flat channel heat flux.

inclined ribs. Both geometrical configurations present a maximum heat flux for $\alpha = 60$.

CHAPTER 7
CONCLUSIONS

Direct numerical simulations have been performed for a turbulent channel flow with turbulators on the walls. Results showed that the segmented V-shaped configuration is the most efficient in transporting heat out of the wall compared with continuous V-shaped ribs. On the other hand, the total drag of the segmented V-shaped configuration decreases. This means that the overall thermal performance ($\frac{Heatflux}{drag}$)of the segmented V-shaped turbulators is higher than that for continuous V-shaped turbulators. This overall increase in thermal performance is due to the changes of the flow structure inside the cavity, the weakening of the recirculation behind each rib element, the reduction of the area normal to impinging flow and the increase in flow momentum inside the cavity caused by the presence of the gap in the turbulator. This is further corroborated by the turbulence intensity in the channel. In fact, the turbulence intensity in the normal and streamwise direction is higher for the segmented V-shaped turbulators in most of the domain, which is consistent with the increase in heat transfer. The weakening of the vortical structure behind the rib is observed in fig. 4–7 and the effects are reflected in the downstream pressure profile (fig. 4–13) and the near wall heat flux.

For one wall V-shaped ribbed channels a decrease in heat transfer and total drag is found. Similar results were observed by Tanda [32] when he compared the heat transfer and friction factor for 45 degrees inclined turbulators on one wall and both walls. The flow redistribution to the upper part of the channel (near the flat wall) cause a non-linear reduction of the total drag and heat transfer. This configuration may offer a better thermal performance due to the fact that less pumping power is needed to drive the flow through one wall ribbed channels.

In addition, numerical results show that there is dependency of the angle between the flow and the turbulators. When the angle of the turbulators is $\alpha = 60$ the heat flux is maximum for both inclined and V-shaped turbulators. Similar results were observed experimentally, as summarized by Han et. al. [22]. Similarly to the comparison between one wall and both walls V-shaped channels, the cost of augmenting the heat transfer is an increase in drag caused by the change of the flow structure and the interaction between the rough wall and the outer layer.

Figures 7–1,7–2,7–3 show a summary of the results of all the geometries studied for this thesis. Overall, the geometrical configuration with the highest heat transfer augmentation is the $w/k = 3$ segmented V-shaped configuration. Moreover, the geometrical configuration which offers the best thermal performance is inclined turbulators with a pitch to height ratio $w/k = 5$ and inclined at $\alpha = 45$ degrees.

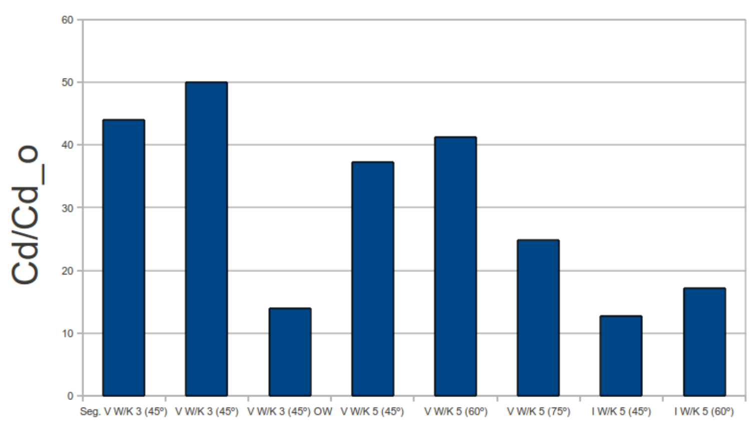

Figure 7–1: Drag coefficient normalized with respect to the flat channel of each configuration. $Re_c = 10400$

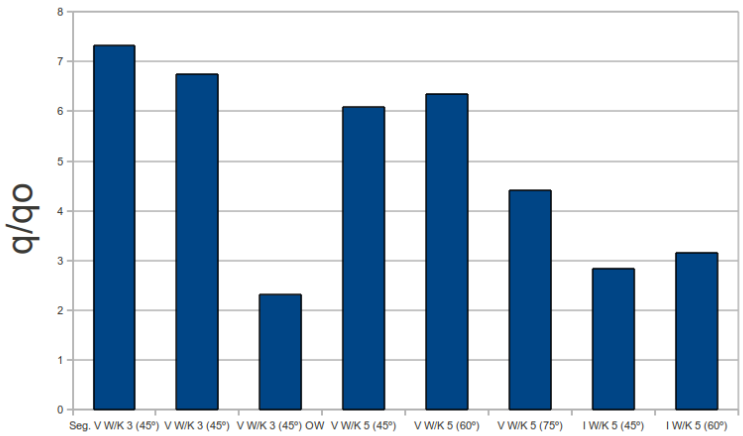

Figure 7–2: Heat transfer augmentation normalized with respect to the flat channel of each configuration. $Re_c = 10400$

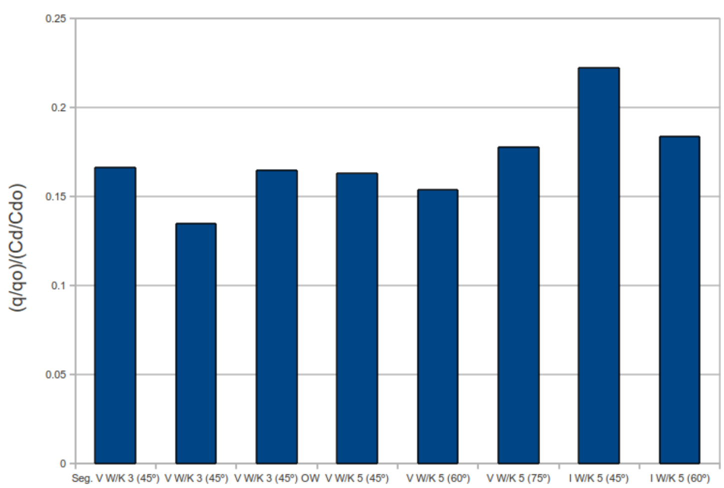

Figure 7–3: Thermal performance normalized with respect to the flat channel of each configuration. $Re_c = 10400$

CHAPTER 8
FUTURE WORK

It will be of interest to find an optimum gap size and to check if the segmented V-shaped turbulators are more efficient at others w/k ratios. Also, previous investigators (for example Leonardi et.al [25]) have found that, for square bars, there is a peak in heat transfer near the region of flow reattachment. Since for one wall turbulators there is no ejections coming from the top wall, as study is needed to determine if others w/k ratios are more efficient in transporting heat inside the channel.

APPENDIX A
λ_2 METHOD

This appendix describes in detail the computation process of the λ_2 method

A.1 DESCRIPTION

The computation of the λ_2 was done with one main program (*lambdampi.f*) and two subroutines. The main program is where the DNS output data and grid are read. Is in the main program, where tensors S and Ω are constructed. Physically, the tensor S and Ω are the strain rate and vorticity tensor. When both terms are squared and summed, the result is a symmetric and real tensor that only have real eigenvalues. A vortex core is present when the second eigenvalue is less than zero. The vortex cores can be observed with Iso-surfaces with a specified second eigenvalue less than zero.

Two subroutines are called in addition to the main program. The *mmult* is the subroutine which squares both tensors. The *eigen* subroutine finds the three eigenvalues of the $S^2 + \Omega^2$ tensor by the use of the QR method. The source code was written in *FORTRAN* and was parallelized with MPI to accelerate the process of computation. It was compiled using *mpif90* with *-r8* options. The parallelization was needed due to the large number of data (24 million points or 1 GB) and computational cost of the QR method.

A.1.1 lambdampi.f

This is the main program. Five different files are needed in order to run the executable: *input.d*, $average\_field\_tin\_tfin$, *xgrid.plo*, *ygrid.plo* and *zgrid.plo*.

input.d: Is where the initial and final timestep are prescribed. For example, if the average field goes from the timestep 1000 to 1500, this file must look like:

```
1000,1500     tin,tfin
```

average_field_tin_tfin: This is an average field that must be generated if desired to compute the λ_2 for the average velocities. The average field is generated for general post-processing use such as the computation of statistical properties or translating the data to *vtk* for visualization purposes. If it is desired to compute the λ_2 for an instantaneous field, the data read source code lines have to be changed and the *input.d* will be different.

Data read source code:

```
Code:
nfil=20
      write(pisc,21) my_node
   21 format(i2.2)
      write(ini,22) tin
      write(fini,22) tfn
   22 format(i4.4)
      filcos='average_field'//pisc//'_'//ini//'_'//fini
      Write(*,*) 'reading average field'
      Write(*,*) filcos
      open(nfil,file=filcos,form='unformatted')
      read(nfil)n1m,n2do,n3m
      write(*,*) n1m,n2do,n3m
      read(nfil)(((qr(k,j,i,1),i=1,n1m),j=0,n2do+1),k=1,n3m),
     1          (((qr(k,j,i,2),i=1,n1m),j=0,n2do+1),k=1,n3m),
     1          (((qr(k,j,i,3),i=1,n1m),j=0,n2do+1),k=1,n3m),
     1          (((rhor(k,j,i),i=1,n1m),j=0,n2do+1),k=1,n3m)
```

```
close(nfil)
```

xgrid.plo, ygrid.plo & zgrid.plo: These are the grid coordinates which are generated by the DNS run.

ygrid.plo sample:

```
  1  -.997500E+00  -.100000E+01  0.500000E-02
  2  -.992500E+00  -.995000E+00  0.500000E-02
  3  -.987500E+00  -.990000E+00  0.500000E-02
  4  -.982500E+00  -.985000E+00  0.500000E-02
  5  -.977500E+00  -.980000E+00  0.500000E-02
  .    .........    ..........    ..........
192  0.997500E+00  0.995000E+00  0.500000E-02
```

After reading and diving the grid in computational layers, it is proceeded to the computation of the velocity gradients.

A *Do loop* was needed to compute the eigenvalues at all grid points. The first step in calculating the strain rate and vorticity tensor is to compute the mean rate-of-displacement tensor $d_{i,j}$ (A.1):

$$d_{ij} = \frac{\partial u_i}{\partial x_j} = \begin{vmatrix} \frac{\partial u}{\partial x} & \frac{\partial u}{\partial y} & \frac{\partial u}{\partial z} \\ \frac{\partial v}{\partial x} & \frac{\partial v}{\partial y} & \frac{\partial v}{\partial z} \\ \frac{\partial w}{\partial x} & \frac{\partial w}{\partial y} & \frac{\partial w}{\partial z} \end{vmatrix} \tag{A.1}$$

```
Code:
diff(1,1)=(qr(i+1,j,k,3)-qr(i,j,k,3))/(x(i+1)-x(i))
diff(2,1)=(qr(i+1,j,k,2)-qr(i,j,k,2))/(x(i+1)-x(i))
```

```
diff(3,1)=(qr(i+1,j,k,1)-qr(i,j,k,1))/(x(i+1)-x(i))
diff(2,2)=(qr(i,j+1,k,2)-qr(i,j,k,2))/(y(j+1)-y(j))
diff(3,2)=(qr(i,j+1,k,1)-qr(i,j,k,1))/(y(j+1)-y(j))
diff(1,2)=(qr(i,j+1,k,3)-qr(i,j,k,3))/(y(j+1)-y(j))
diff(2,3)=(qr(i,j,k+1,2)-qr(i,j,k,2))/(z(k+1)-z(k))
diff(3,3)=(qr(i,j,k+1,1)-qr(i,j,k,1))/(z(k+1)-z(k))
diff(1,3)=(qr(i,j,k+1,3)-qr(i,j,k,3))/(z(k+1)-z(k))
```

Then, the strain rate (A.2) and vorticity tensor (A.3) are constructed:

$$s_{ij} = (d_{ij} + d_{ji})/2 \tag{A.2}$$

$$\Omega_{ij} = (d_{ij} - d_{ji})/2 \tag{A.3}$$

S

```
Code:
Do ii=1,3
Velgrad(1,ii)=(diff(1,ii)+diff(ii,1))/2
enddo
Do ii=1,3
Velgrad(2,ii)=(diff(2,ii)+diff(ii,2))/2
enddo
Do ii=1,3
Velgrad(3,ii)=(diff(3,ii)+diff(ii,3))/2
enddo
```

$\Omega:$

```
Code:
Do ii=1,3
omega(1,ii)=(diff(1,ii)-diff(ii,1))/2
enddo
```

```
Do ii=1,3
omega(2,ii)=(diff(2,ii)-diff(ii,2))/2
enddo
Do ii=1,3
omega(3,ii)=(diff(3,ii)-diff(ii,3))/2
enddo
```

The following step is to square both tensors (A.2 & A.3) with the subroutine *mmult*. Once S^2 and Ω^2 are computed, it is proceeded to sum both arrays. The resulting array is the input for the subroutine *eigen*. Finally the second eigenvalue is obtained by eliminating the maximum and minimum values of the *eigen* subroutine output. This data is then written to *.vtk* for visualization.

```
Code:
Call mmult(Velgrad,Velgrad,Velgradm,3,3,3)
Call mmult(omega,omega,omegam,3,3,3)
...
Velgrad(ii,jj)=Velgradm(ii,jj)+omegam(ii,jj)
...
call eigen((Velgrad),reig)
...
rmaxi=reig(1)
rmin=reig(3)
Do ii=1,3
   if (reig(ii).ge.rmaxi) then
   rmaxi=reig(ii)
   endif
   if (reig(ii).le.rmin) then
   rmin=reig(ii)
```

```
   endif
enddo


Do ii=1,3
   if (reig(ii).lt.rmaxi.and.reig(ii).gt.rmin) then
   remed=reig(ii)
   endif
   enddo
```

A.1.2 mmult.f

The subroutine mmult is for matrix multiplication. The two inputs are the arrays to be multiplied.

```
mmult(Array_A,Array_B,Output_Array,Array_A_rows,Common_Dimension,Array_B_Columns)
```

A.1.3 eigen.f

This is the subroutine used to compute real eigenvalues of a three by three matrix using the QR method. The inputs is a three by three array and the output is a array of a dimension of three. To details about the numerical method refer to Joe D. Hoffman [23] book. Since the QR method is an iterative process, the computation has to be repeated until is satisfies certain tolerance. For this thesis, the tolerance used to achieve numerical convergence was $1e-10$. **This subroutine works only for three by three matrices with real eigenvalues**.

```
eigen(Array_A,eigenval_array)
```

A.2 FLOW CHART

Figure A–1 is a flowchart of the previously explained method.

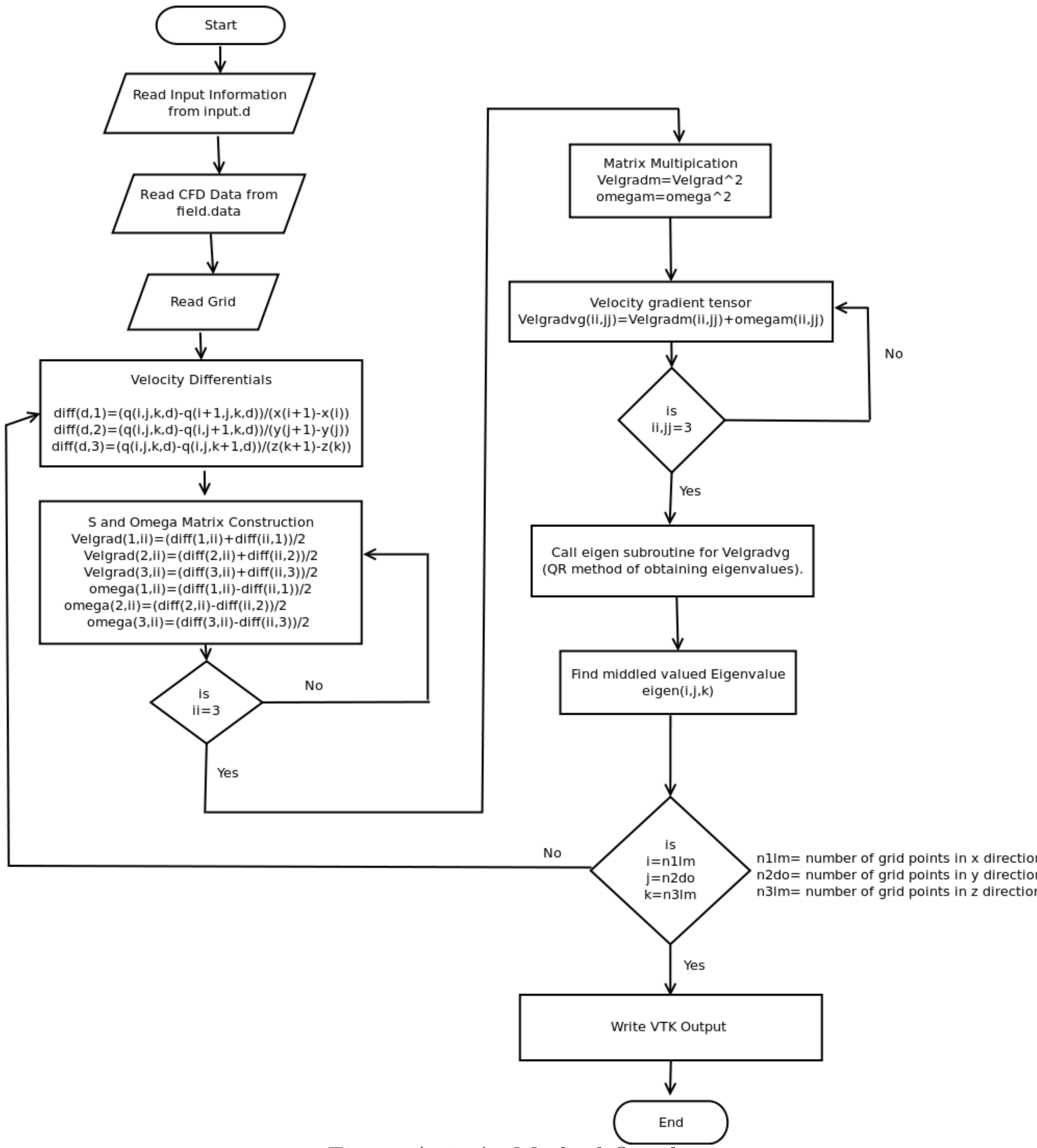

Figure A–1: λ_2 Method flowchart

A.3 VISUALIZATION METHOD

The software *Paraview* was used to visualize the iso-surfaces of the resulting eigenvalues at each point. *Paraview* was used because is a free and open source visualization toolkit designed to render large datasets. First, *Paraview* has to be run. Then, *.vtk* output has to be opened from the program GUI. After the data is loaded the filter *Contour* has to be selected. Finally, in the object inspector, the desired iso-surface value has to be specified (must be less than zero) and rendered. Refer to Fig. A–2 for the step by step process as seen from the *Paraview* console.

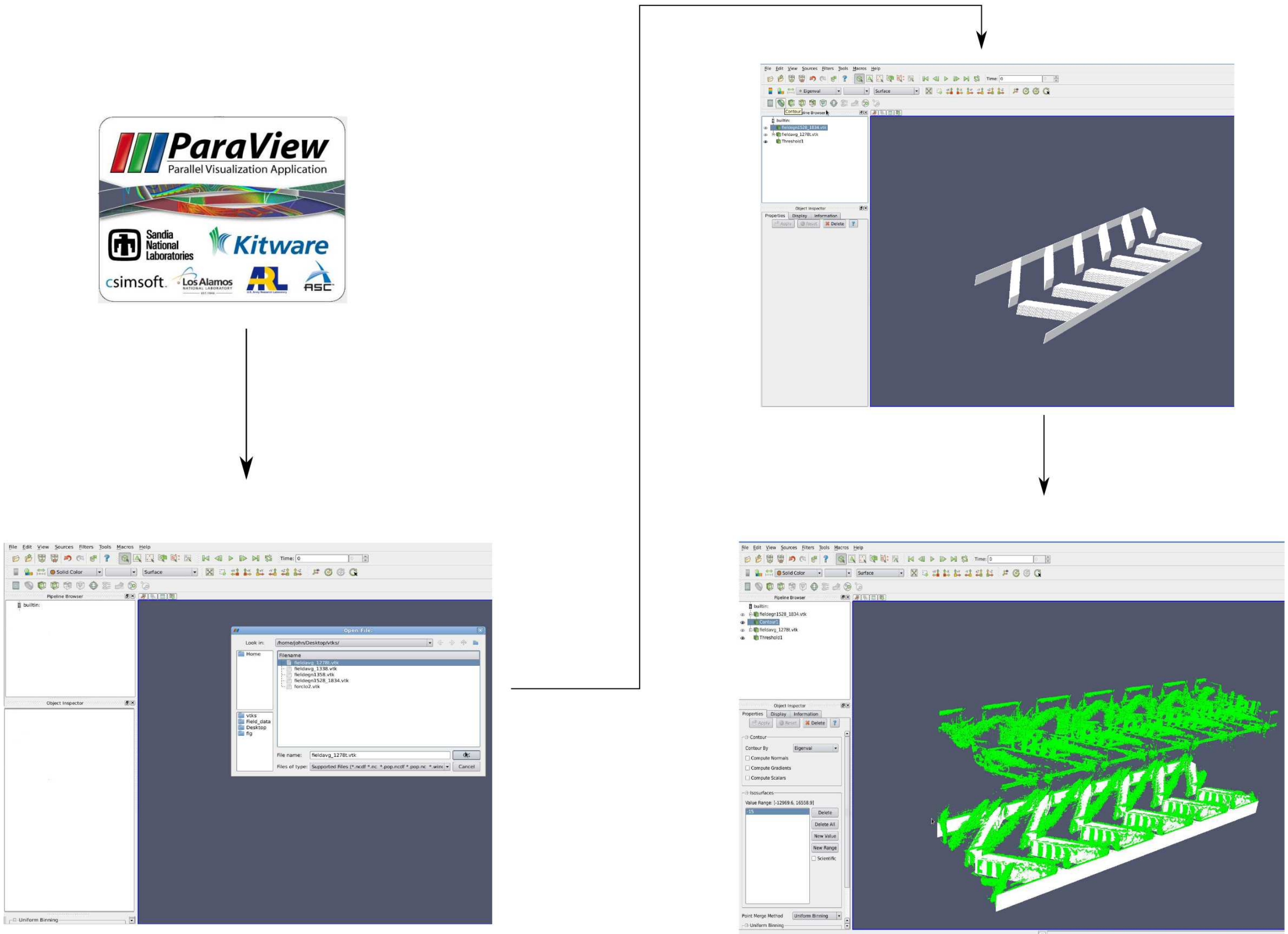

Figure A–2: Paraview Flowchart

REFERENCE LIST

[1] J.C Han (1984). Heat transfer and friction in channels with two opposite rib-roughened walls. *ASME J. Heat Transfer* vol. 106, pp. 851-861.

[2] J.C. Han (1988). Heat transfer and friction characteristics in rectangular channels with rib turbulators.*ASME J. Heat Transfer* vol. 110, pp.321-328.

[3] S. K. Robinson (1990). Coherent Motions in the Turbulent Boundary Layer.*Turbulent Boundary Layers* vol. 23, pp.601-639.

[4] J.C. Han (1993). Augmented heat transfer in square channels with parallel, crossed and V-shaped angled ribs. *ASME J. Heat Transfer* vol.113, pp.2013-2020.

[5] X.gao, B. Sunden (2001). Heat transfer distribution in rectangular ducts with V-shaped ribs. *Heat Mass Transfer* vol.37, pp.315-320.

[6] G. Tanda (2004). Heat transfer in rectangular channels with transverse and V-shaped broken ribs. *International Journal of Heat and Mass Transfer* vol.47, pp.229-243.

[7] S. Leonardi, P. Orlandi, L. Djenidi b, R.A. Antonia (2004). Structure of turbulent channel flow with square bars on one wall. *International Journal of Heat and Fluid Flow* vol. 25, pp.384-392.

[8] S.Y. Won, P.M. Ligrani (2004). Comparisons of flow structure and local Nusselt numbers in channels with parallel and crossed-rib turbulators. *International Journal of Heat and Mass Transfer* vol. 47, pp.1573-1586.

[9] Mark F. Tachie, Samuel S. Paula, Martin Agelinchaaba and Mohammad K. Shahb (2009). Structure of turbulent flow over 90 degrees and 45 degrees transverse ribs. *Journal of Turbulence* vol. 10, No. 20, pp.1-23.

[10] J. Jeong & H. Hussain (1995). On the identification of a vortex.*J. Fluid Mechanics* vol.285, pp.69-94.

[11] C.R. Smith & S.P. Metzler (1983). Observation of streamwise rotation in the near wall region of a turbulent boundary layer. *Phys. Fluids* vol. 26, pp.241-252.

[12] J.A. Clark & E. Markland (1971). Flow visualization in turbulent boundary layers. *L. Hydraulic Div.* ASCE vol. 97, pp.1653-1664.

[13] M.R. Head & P. Bandyopadhyay (1981). New aspects of turbulent boundary layer structure.*J. Fluid Mechanics* vol.107, pp.297-338.

[14] L. Djenidi, R. Elavarasan & A. Antonia (1999). The turbulent boundary layer over transverse square cavities, *J. Fluid Mech.* vol. 395, pp.271-294.

[15] S. Leonardi,P. Orlandi, R.A Antonia (2007). Properties of d- and k-type roughness in a turbulent channel flow. *Physics of Fluids* vol. 19, id. 125101.

[16] L. Keirsbuick, L. Labraga, A.Mazouz & C. Tournier (2002). Surface Roughness Efects on Turbulent Boundary Layer Structures. *J. Fluid Engineering* vol. 124, pp.127-135.

[17] D. Wilkie (1966). Forced convection heat transfer from surfaces roughened by transverse ribs. *Proceesings of the Third International Heat Transfer Conference* vol.1, Chicago, USA, pp.1-19.

[18] J.C Han, L.R. Glickmann, W.M Rohsenow (1978). An investigation of heat transfer and friction for rib-roughened surfaces. *Int. J. Heat Mass Transfer* vol. 21, pp.1143-1156.

[19] J.C. Han & Y.M Zhang (1992). High performance heat transfer ducts with parallel broken and V-shaped broke ribs. *Int. J. Heat Mass Transfer* vol. 40, pp.2525-2537.

[20] H. T. Kim, S.J. Kline, W.C. Reynolds (1971). The production of turbulence near a smooth wall in a turbulent boundary layer. *J. Fluid Mech.* vol. 50, pp.133-160.

[21] Wray A.A., (1987) Very low storage time-advancement schemes. *NASA Ames Research Center, Moffet Field, California: Internal Report*

[22] J. C. Han, Sandip Dutta and Srinath V Ekkad, *Gas Turbines Heat Transfer and Cooling Technology*, Taylor & Francis 2000

[23] Joe D. Hoffman, *Numerical Methods for Engineers and Scientists*, CRC Press; 2^{nd} edition 2001

[24] Leonardi, S., Orlandi, P., Smalley, R.J., Djenidi, L. & Antonia, R.A. (2003). Direct numerical simulations of turbulent channel flow with transverse square bars on one wall. *J. Fluid Mech.* vol. 491, pp.229-238.

[25] Leonardi, S., Orlandi, P. & Antonia, R.A. (2007). Heat Transfer in a Turbulent Channel Flow with Roughness, 5th International Symposium on Turbulence and Shear Flow Phenomena TU Munich - 27-29 August 2007.

[26] Orlandi, P. (2000) Fluid flow phenomena, a numerical toolkit. *Kluwer Academic Publishers.*

[27] Orlandi P. & Leonardi S. (2006) DNS of turbulent channel flows with two and three-dimensional roughness. *Journal of Turbulence* vol. 7, id. N53.

[28] Leonardi S. (2004) Structure of turbulent channel flow with square bars on one wall. *International J. of Heat and Fluid Flow* vol. 25, pp.384-392.

[29] P. Moin, J. Kim (1985) The structure of the vorticity field in turbulent channel flow. Part 1. Analysis of instantaneous field and statistical correlations. *J. Fluid Mech.* vol. 155, pp.441-464.

[30] Perry A. E., Shcofield W. H., Joubert P.N. (1969). Rough wall turbulent boundary layers. *J. Fluid Mech.* vol. 37, pp.383-413.

[31] Fadlun E. A., R. Verzicco, Orlandi P., and Mohd-Yusof J. (2000). Combined immersed boundary finite-difference methods for three-dimensional complex flow simulations. *J. Comput. Phys.* vol. 161, part 1, pp.35-60.

[32] Giovanni Tanda (2011). Effect of rib spacing on heat transfer and friction in a rectangular channel with 45 angled rib turbulators on one/two walls. *International Journal of Heat and Mass Transfer* vol. 54, pp.1081-1090.

[33] Jaime A. Toro Medina, Direct Numerical Simulation Of Turbulent Channel Flow With V-Shape Turbulators. *University of Puerto Rico Mayaguez Campus* 2010.

[34] J. Cui, V.C Patel, C-L Lin (2003). Large-eddy simulation of turbulent flow in a channel with rib roughness, *International J. of Heat and Fluid Flow* vol. 24, pp.372-388.